Journal of Structural Geology 113 (2018) 134–154

Contents lists available at ScienceDirect

Journal of Structural Geology

journal homepage: www.elsevier.com/locate/jsg

Structural and hydrothermal evolution of a strike-slip shear zone during a ductile-brittle transition, Sierra Nevada, CA

Sean M. Hartman[a,*], Scott R. Paterson[a], Gregory J. Holk[b], James D. Kirkpatrick[c]

[a] Department of Earth Sciences, University of Southern California, Los Angeles, CA 90089, USA
[b] Department of Geological Sciences, California State University, Long Beach, CA 90840, USA
[c] Department of Earth and Planetary Sciences, McGill University, 3450 University St., Montreal, QC H2T 2R8, Canada

ARTICLE INFO

Keywords:
Dilational fault jogs
Meteoric-hydrothermal fluids
Brittle-ductile transition
Pseudotachylyte
Oxygen isotopes
Sierra Nevada

ABSTRACT

The incursion of meteoric-hydrothermal fluids into the ductile crust can be evaluated with the stable isotope ratios of minerals in exhumed ductile shear zones, but the incursion mechanisms are yet to be well-demonstrated. Field structural and microstructural relations and regional oxygen isotope patterns from an exhumed, Late Cretaceous shear zone-fault system in the central Sierra Nevada, CA, are used to reconstruct the deformation history and develop insights into fluid incursion mechanisms. A ductile-to-brittle transition was partially accommodated by a strike-slip duplex involving flexural slip-accommodated folding along faults. Two main NNW-striking brittle fault strands overlap, the northern fault curves into the southern fault, which is sealed by a > 4 m wide composite quartz vein. Based on structural relationships, we interpret the transition from ductile to brittle deformation to have occurred during cooling of the adjacent Late Cretaceous Tuolumne Intrusive Complex. Quartz-sealed fault veins in the pendant have $\delta^{18}O$ values ranging from −3.2 to 14.5‰, and are interpreted to have precipitated partially or fully from meteoric-hydrothermal fluids, including quartz veins that have been recrystallized. The lowest values are only found within the region of the jog. The $\delta^{18}O$ values for pseudotachylyte matrix in one sample from this fault system are $\delta^{18}O = 3.3‰$, $\delta^{2}H = -137‰$. Together, these data indicate meteoric-hydrothermal incursion into a deforming, seismogenic brittle-ductile transition.

1. Introduction

Fluids have profound effects on fault behavior due to their control on effective stress and thus fluid pressure-dependent rock strength and failure (Dieterich, 1974). Earthquake magnitude potential increases with depth in the seismogenic crust because of the increase in rock strength (Sibson, 1982), which may peak near the brittle-ductile transition (Behr and Platt, 2014). Fluids can affect seismic behavior in the seismogenic zone by promoting aseismic creep through pressure solution mechanisms (Gratier et al., 2011), and below the seismogenic zone by inducing tremor (Peng and Gomberg, 2010; Wech et al., 2012). Mineral precipitation from circulating fluids may also change the permeability of fault zones, controlling the earthquake cycle (Sibson et al., 1988). It has also been suggested that brittle mechanisms that facilitate fluid flow are important precursors of ductile shear zones in the middle crust (Mancktelow and Pennacchioni, 2005; Soden et al., 2014; Spruzeniece and Piazolo, 2015) because they can accelerate dynamic quartz recrystallization and metamorphic phyllosilicate growth, which weakens the rocks (Fusseis and Handy, 2008).

There are a number of possible sources of fluids that interact with faults. The source (e.g. magmatic, metamorphic, mantle, or meteoric), in addition to the mechanism by which it is allocated to the fault, strongly influences the fluid's volume and flux rate. Hence, the source may indirectly influence fault mechanics. Meteoric fluids are one fluid source whose volume within the crust may be limited only by the crust's permeability, porosity, hydraulic gradient, and open connection to the surface in many places. If a hydrological connection between the surface and ductile parts of the crust can be established, it could potentially have a profound effect on the character of fault zone seismicity, strength, and structural evolution.

Stable isotope geochemistry has been used to demonstrate incursion of meteoric-hydrothermal fluids into ductile crust (e.g. Morrison, 1994; Holk and Taylor, 2007; Gébelin et al., 2011; Holk et al., 2017). They have revealed the incursion of meteoric-hydrothermal fluids into compressed ductile shear zones (e.g. Lobato et al., 1983; Menzies et al., 2014). Surface-derived hydrothermal fluids may descend from brittle faults into the deeper ductile crust by dip-slip juxtaposition of cooler shallow crust with hotter deep crust (McCaig, 1988) via suction pumping, a process in which pre-seismic microcracks dilate, drawing in fluids, which are subsequently expelled during the co-seismic phase

* Corresponding author.
E-mail address: smhartma@usc.edu (S.M. Hartman).

https://doi.org/10.1016/j.jsg.2018.05.010
Received 17 November 2017; Received in revised form 10 May 2018; Accepted 13 May 2018
Available online 01 June 2018

when local dilational stresses are relaxed, closing formerly open cracks (Sibson, 1981). Minerals demonstrating plastic recrystallization microstructures from an exhumed part of the transpressive Alpine fault in New Zealand have calculated fluid $\delta^{18}O$ values based on recrystallized mineral $\delta^{18}O$ values as low as −4‰ (Lobato et al., 1983) and −9‰ (Menzies et al., 2014). These low $\delta^{18}O$ values imply meteoric-hydrothermal fluids (Craig, 1961) flowed through the brittle-ductile transition.

Extension in dilational jogs, which accommodates the offset in the corresponding flanking strike-slip faults, may act as zones of co-seismic suction that draw in fluids from the surrounding rock, leading to local implosive brecciation and hydrothermal boiling (Sibson, 1987). The Martha Hill lode system in New Zealand is an example of an ~1 km wide fossil dilational jog system, whose vein-fill textures and fluid inclusion assemblages indicate brecciation and boiling in the dilational faults (Brathwaite et al., 1986). They related the boiling to suction forces during co-seismic dilation and postulated that such processes could occur at up to 10 km depth.

Theoretical models describing mechanisms of meteoric-hydrothermal fluid incursion into tectonically compressed ductile crust (e.g. McCaig, 1988) have been supported by stable isotope studies demonstrating meteoric-hydrothermal interaction with recrystallized minerals in thrust (e.g. Lobato et al., 1983) and transpressive (e.g. Menzies et al., 2014) shear zones. However, field relationships between the stable isotope evidence of such fluids and the specific structures that directly permitted their descent have yet to be well-demonstrated. In this paper, we present mapping from km to m scales as the architectural blueprints of the exhumed brittle-ductile transition of a locally dilated, seismogenic, dextral strike-slip fault zone in the central eastern Sierra Nevada, California. Our mapping and structural analyses suggest that the brittle fault system was preceded by ductile shearing, and the transition was caused by cooling in response to the conclusion of magma emplacement in the Tuolumne Intrusive Complex (TIC) to the west of the Saddlebag Lake pendant. Recrystallized quartz veins in the Sawmill Canyon area were precipitated in equilibrium with a fluid partially or fully composed of meteoric-hydrothermal water (Compton et al., 2017). The purpose of this paper is to address the following questions: 1) How did the structures within the shear zone evolve as deformation mechanisms transitioned from quasiplastic (ductile) to frictional (brittle)? 2) What were the sources and spatial distribution of hydrothermal fluid flow in the western Saddlebag Lake pendant and TIC? 3) What structures permitted meteoric-hydrothermal fluid flow at the brittle-ductile transition? 4) Did earthquakes occur during meteoric-hydrothermal fluid flow?

2. Geologic setting

2.1. Regional background

The Mesozoic Sierra Nevada Batholith is an ~600 km long continental arc segment (Fig. 1) related to a Mesozoic subduction system that spanned the western boundary of the North and South American continental margins, part of which is still active in the Pacific northwest region of North America. Sierran arc magmatism spanned much of the Mesozoic and culminated with a regional shutoff in the Late Cretaceous (Ducea, 2001). In the central Sierra Nevada batholith, Cretaceous magmatism formed the Tuolumne Intrusive Complex (TIC), a normally zoned, composite magmatic complex with an area of ~1100 km^2 at the surface. The TIC was emplaced between 95 and 85 Ma (e.g. Kistler and Fleck, 1994; Coleman et al., 2004; Miller et al., 2007) into older Mesozoic arc-related intrusions and Paleozoic and Mesozoic metasedimentary and metavolcanic units of the Saddlebag Lake and Ritter Range roof pendants (e.g. Huber et al., 1989; Schweickert and Lahren, 1993, 2006). Magma sources for the TIC were dominated by recycling of lower crust and mantle, indicated partially by zircons with $\delta^{18}O$ values only slightly elevated above typical mantle values (Lackey et al., 2008).

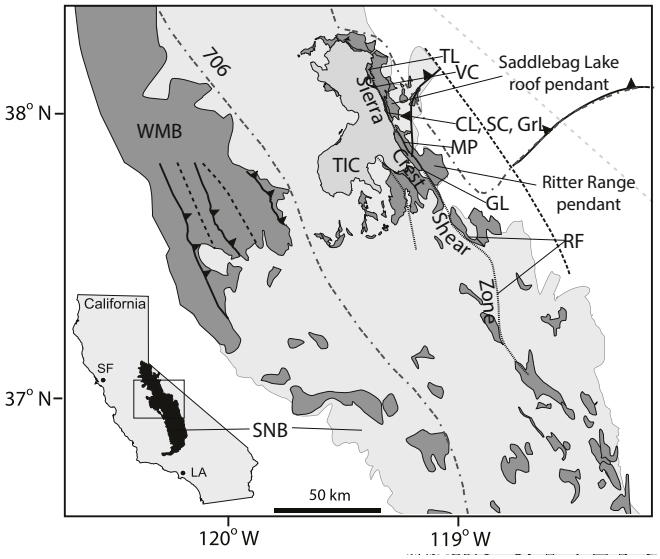

Fig. 1. Location of the Sierra Nevada batholith (SNB) in California (bottom left, LA = Los Angeles, SF = San Francisco, after Cao et al., 2016), with the central part of the batholith outlined in the inset. In the inset, the batholith intrudes the Western Metamorphic Belt (WMB) in the west, and the Tuolumne Intrusive Complex (TIC) intrudes eastern roof pendants with Paleozoic rock units. Segments of the Sierra Crest shear zone are located along the line with the shortest dashes (TL = Twin Lakes, VC = Virginia Canyon, CL = Cascades Lake, SC = Sawmill Canyon, Grt = Granite Lakes, MP = Mono Pass, GL = Geml Lake, RF = Rosy Finch).

Emplacement of the TIC coincided with ductile dextral, transpressive shearing in the central Sierra Nevada batholith during the Late Cretaceous (Tikoff and Teyssier, 1992; Tikoff, 1994; Tobisch et al., 1995; McNulty, 1995; Greene and Schweickert, 1995; Tikoff and Greene, 1997; Tikoff and de Saint Blanquat, 1997; Sharp et al., 2000; Bentley, 2004; Tikoff et al., 2005; Horsman et al., 2008; Jiang and Bentley, 2012; Paterson and Memeti, 2014; Paterson et al., 2014; Cao, 2015; Cao et al., 2015; Nadin et al., 2016; Compton et al., 2017).

2.2. Previous results from the Saddlebag Lake pendant

2.2.1. Setting

The Saddlebag Lake roof pendant is one of a series of pendants preserved in the eastern central Sierra Nevada Batholith (Figs. 1 and 2), bordering the eastern boundary of Yosemite National Park. It is truncated to the west by the TIC and on the north and east by older Mesozoic plutons. Its southern boundary is covered by Quaternary alluvium, south of which similar rocks continue in the Northern Ritter Range pendant. Rocks in the western Saddlebag Lake pendant stratigraphically young to the west (Schweickert and Lahren, 2006; Paterson and Memeti, 2014). Units in the Granite Lakes, Sawmill Canyon, and Cascades Lake segments of the SCSZ increase in age to the east, and include a sliver of Cretaceous rhyolite (~95–115 Ma; Paterson and Memeti, 2014; Cao, 2015), a Jurassic unit ("Sawmill Canyon Sequence"), consisting of metamorphosed conglomerate, pelite, limestone, siltstone, sandstone, and volcaniclastics (< 180 Ma, Paterson and Memeti, 2014; Cao, 2015), and a > 1 km thick Triassic metavolcanic unit ("Koip Sequence"), consisting of metamorphosed rhyolite, dacite, and andesite (~235–219 Ma). Rocks to the east are as old as Paleozoic (Attia et al., In Press).

Mineral assemblages in Saddlebag Lake pendant rocks and pressure-corrected geothermometry in magmatic intrusions demonstrate older greenschist metamorphism overprinted by a contact aureole that grades from amphibolite to greenschist facies metamorphic assemblages away from the intrusions (Brook, 1977; Albertz, 2006; Schweickert and Lahren, 2006). Calculated maximum metamorphic host rock

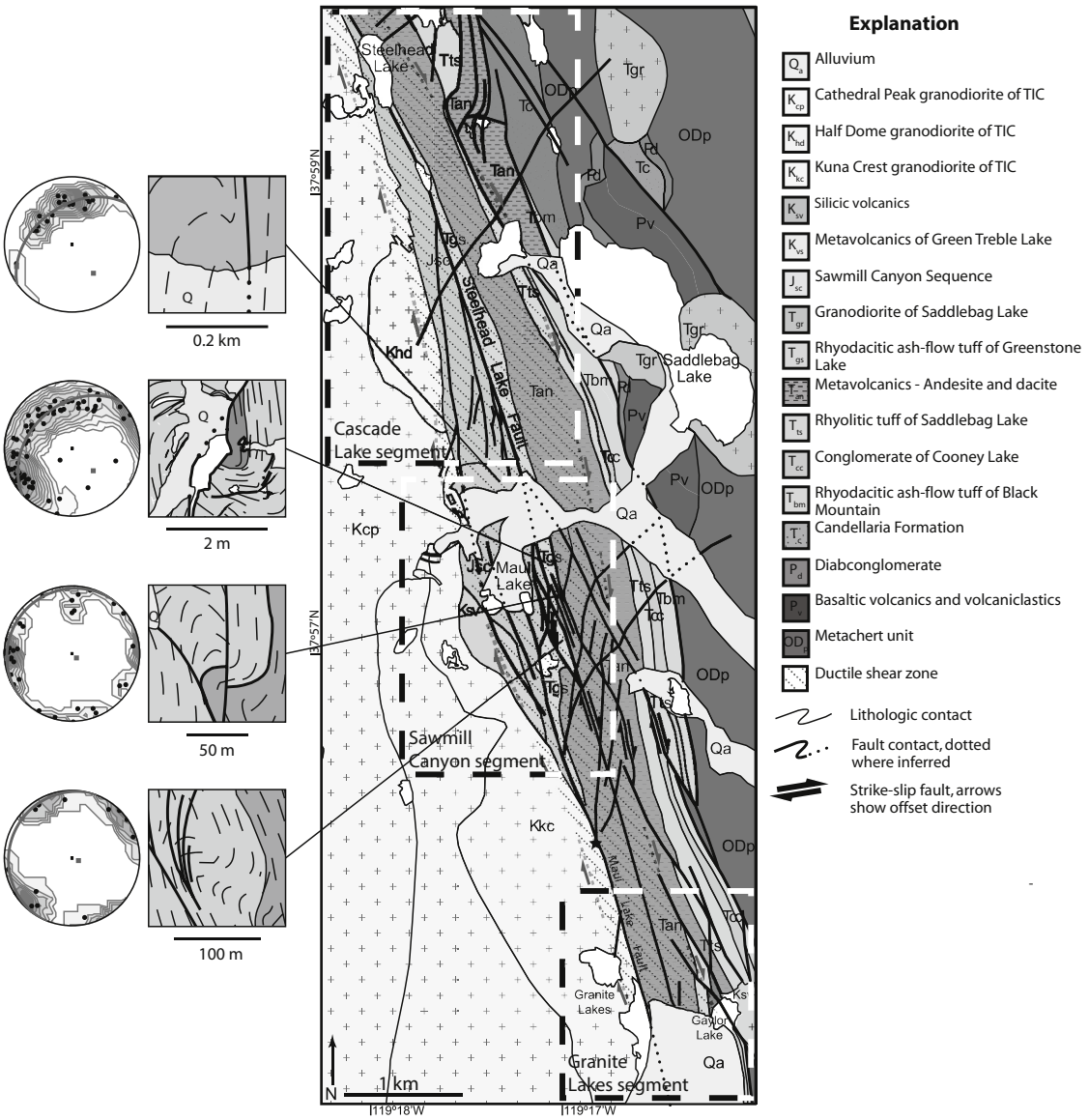

Fig. 2. Geologic map of the Cascades Lake (north), Sawmill Canyon (central), Granite Lakes (south) segments of the Sierra Crest Shear Zone. Stratigraphy youngs to the west and is truncated to the west by the Tuolumne Intrusive complex (TIC). Structures indicate a dextral ductile shear zone overprinted by a brittle fault network consisting of clusters of shear zone subparallel and oblique faults. Maps of four folds are shown in detail to the left of the map main map. The top fold deforms the metavolcanic rocks in Sawmill Canyon whose geologic history is poorly constrained. The second fold from the top is shown in detail in Fig. 9, and the bottom two folds are shown in detail in Fig. 4. Stereonets show subhorizontal girdles formed by poles to planes of metamorphic foliation defining the folds. From top to bottom, the calculated girdles are respectively 233/44 (n = 20), 227/37 (n = 76), 224/7 (n = 35), and 202/8 (n = 14). The black star shows the location of pseudotachylyte sample G3, shown in Fig. 14.

temperatures > 700 °C indicate that host rocks approached metamorphic equilibrium with adjacent near-solidus TIC (Paterson et al., 2014). Calculated pluton emplacement depths (~7 km, based on 1.9 kbar, Paterson and Memeti, 2014) are consistent with regional metamorphic grades indicated by andalusite and sillimanite assemblages (Rose, 1957; Memeti et al., 2005; Anderson et al., 2007). Systematic mineralogical changes in host rock westward toward the TIC developed in the presence of water-rich vapor phases at elevated (contact metamorphic) temperatures of 550–670 °C (Kerrick, 1970).

2.2.2. Deformation

The western Saddlebag Lake pendant and eastern TIC are deformed by the Sierra Crest Shear Zone (SCSZ; Tikoff et al., 2005; Bentley, 2004; Jiang and Bentley, 2012; Paterson et al., 2014; Cao et al., 2015). The length of the entire ductile shear zone is likely at least 100 km (Fig. 1), extending from the Twin Lakes segment ~20 km north of Sawmill Canyon (Cao, 2015), to the Rosy Finch segment, ~80 km south of Sawmill Canyon (Tikoff and de Saint Blanquat, 1997). The aligned segments that define the SCSZ, demarcated by the Twin Lakes and Rosy Finch segments, preserve abundant structural and geochronologic evidence for Late Cretaceous, dextral, transpressive shearing (e.g. Greene and Schweickert, 1995; Tikoff and Greene, 1997; Bentley, 2004; Paterson and Memeti, 2014). In the Gem Lake segment, both coaxial, subvertically stretched metamorphic minerals, and non-coaxial, dextrally sheared metamorphic minerals overlap in age with each other (Sharp et al., 2000), and with a dextrally sheared dike in the Cascades Lake segment in the 20 Lakes Basin area (Figs. 2 and 3; Paterson and Memeti, 2014). In the Rosy Finch segment of the SCSZ, ductile shearing of cooling plutons from hornblende $^{40}Ar/^{39}Ar$ closure temperature (580–490 °C; Harrison, 1981) to biotite $^{40}Ar/^{39}Ar$ closure temperature

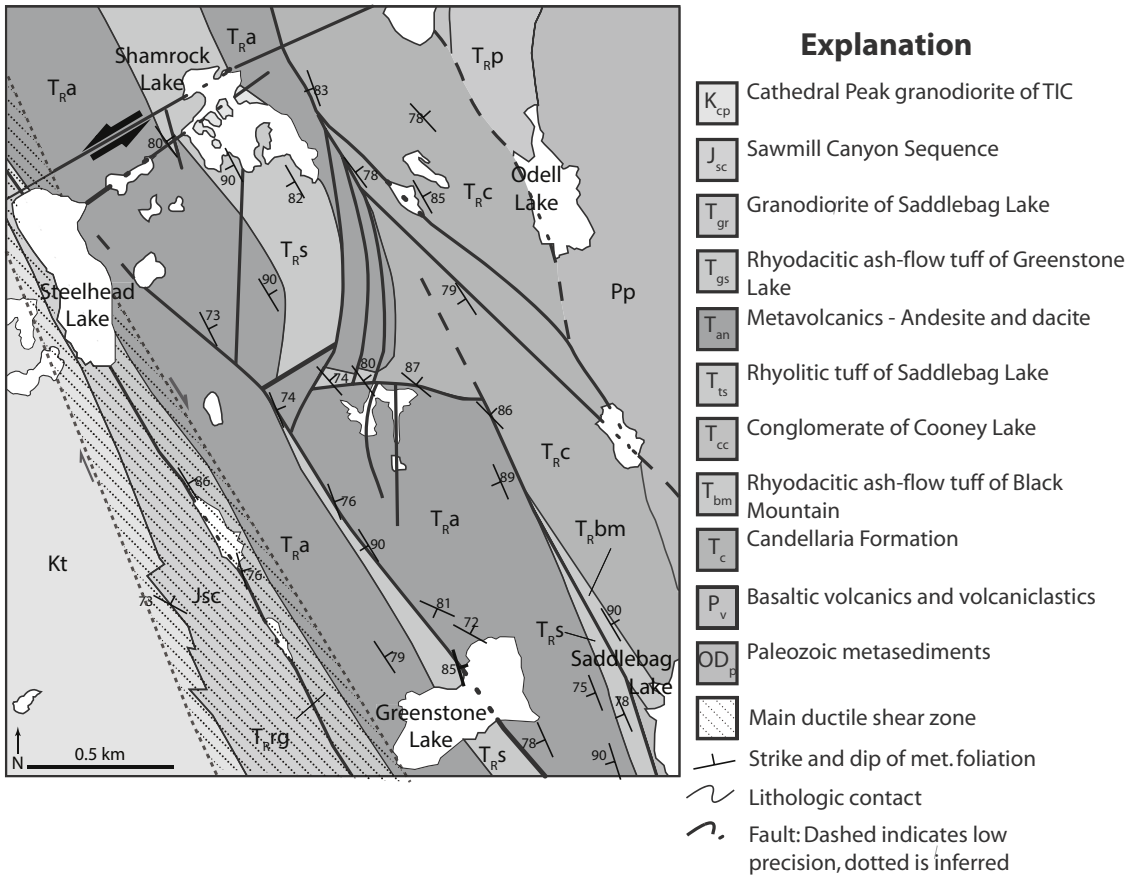

Fig. 3. Geologic map of the 20 Lakes Basin area with the Cascades Lake segment of the Sierra Crest Shear Zone in the western Saddlebag Lake pendant. The brittle shear zone overprints the ductile shear zone and fault-bound rocks are displaced such that older rocks intersect structurally higher and younger rocks along strike. The curved, fault-bound rhyolite and andesite slivers define a duplex that repeats the andesite package.

(345–280 °C; Harrison et al., 1985) occurred between ca. 87 (hornblende) and 80 (biotite) Ma, and deformed the 85 Ma Mono Creek pluton (Tobisch et al., 1995). Similarly, in the Gem Lake segment, hornblende to biotite closure temperatures occurred from 85 to 80 Ma (Sharp et al., 2000). In the Cascades Lake segment, biotite closure occurred at 84 Ma (Paterson and Memeti, 2014), and in the Virginia Canyon segment (Fig. 1), closure between hornblende and biotite occurred between ca. 86 and 80 Ma (Cao et al., 2015).

Structures comprising the Sawmill Canyon segment of the SCSZ indicate ductile (outcrop scale) deformation (Paterson and Memeti, 2014; Compton et al., 2017). Ductile structures of the shear zone include metamorphic foliation of continuous cleavage defined by aligned micas, elongate quartz and quartz ribbons, spaced cleavage defined by anastomosing muscovite bands and interlayered epidote-rich and epidote-poor bands, asymmetric and imbricated clasts, sigma and delta porphyroblasts, mylonites, S-C fabrics, boudinage, and both asymmetric and isoclinal folds (Compton et al., 2017). Quartz vein microstructures include patchy undulose extinction, irregular grain shapes, subgrain development with variable degrees of recrystallization, sutured grain boundaries, bulging, core and mantle structure, aligned aggregates, interlobate grain boundaries, triple junctions, and dragging structures in parts pinned by muscovite (Compton et al., 2017). Feldspars also have sweeping undulose extinction and rarer subgrain formation. Both quartz and feldspar exhibit recrystallization to equigranular aggregates of subgrains (Compton et al., 2017).

The 95-85 Ma (Kistler and Fleck, 1994; Coleman and Glazner, 1997; Matzel et al., 2005, 2006; Miller et al., 2007) TIC was deformed by the SCSZ during and after its final major stage of intrusion, the 88-85 Ma Cathedral Peak granodiorite, as evidenced by both magmatic and high temperature subsolidus recrystallization (Tikoff et al., 2005). Fabrics on sub-horizontal outcrops include foliation traces, S-C fabrics, minor shear bands, and book-shelf sliding of clusters of K-feldspar megacrysts (Tikoff et al., 2005). The kinematics of these fabrics all indicate dextral shear and are consistent with regional clockwise rotation of fabrics (Tikoff et al., 2005).

Apatite and zircon (U-Th)/He and biotite and hornblende $^{40}Ar/^{39}Ar$ thermochronology and Al-in-hornblende thermobarometry demonstrate that this part of the central Sierra Nevada was exhumed from a depth of 6–8 km at a non-uniform rate (Cecil et al., 2006; Cao et al., 2015, 2016). Regional uplift and erosion between 220 and 80 Ma exhumed the level of the crust represented at the current surface from ~12 km to ~8 km, based on Al-in-hornblende barometry from plutons (Paterson et al., 2014; Cao et al., 2015). Exhumation then increased to 0.3–0.7 km/my during the Late Cretaceous to Early Cenozoic, and slowed to 0.25 km/my at 60 Ma, removing the remaining 6–8 km of overload and exposing this part of the crust at the surface. Calculated emplacement depths from Al-in-hornblende barometry of the currently exposed TIC surface yield depths between 6 and 10 km (Ague and Brimhall, 1988; Webber et al., 2001; Gray, 2003; Anderson et al., 2007; and Cao et al., 2015). Emplacement pressures of 1.9 kbar and 701 °C are revealed by Al-in-hornblende-plagioclase thermobarometry for the Cathedral Peak phase of the TIC near Sawmill Canyon (Paterson and Memeti, 2014; Cao et al., 2015).

Brittle faults were first recognized in the Saddlebag Lake pendant due to interest in Cu, Pb, Zn, Au, and Co deposits (Tucker and Sampson, 1940). Their traces are dotted with mine pits from ca. a century ago. Pseudotachylyte has been recognized as a component of the brittle fault system in the western part of the pendant (Whitesides et al., 2010).

Paterson and Memeti (2014) argued that the brittle fault zones that overprint the ductile shear zones represent a continued stress field imposed on the rocks as hot, plastic deformation mechanisms were replaced by cooler, frictional mechanisms.

Mineral stable isotope studies from hydrothermal veins and host rocks have hinted at focused meteoric-hydrothermal incursion during Late Cretaceous fluid flow in the Saddlebag Lake pendant. All hydrous minerals with $\delta^{18}O < 6‰$ and quartz and plagioclase with $\delta^{18}O < 9‰$, are restricted to the Sawmill Canyon segment of the SCSZ (Lojasiewicz et al., 2016; this study). The $\delta^{18}O$ values from recrystallized quartz veins in the Sawmill Canyon segment of the SCSZ are as low as 2.5‰, and precipitated from fluids with calculated $\delta^{18}O$ values as low as −2.0‰ (Compton et al., 2017).

3. Structural geology

3.1. Geologic maps

3.1.1. Ductile shear zone

The western boundary of the southern Saddlebag Lake pendant, which is juxtaposed with the TIC to the west, is deformed by a ductile shear zone that is overprinted by a brittle fault zone (Fig. 2). The shear zone primarily deforms the youngest rocks comprising the pendant, near the contact with the TIC. The main strand of ductile shear is defined by the highest concentration of outcrops with dextral shear indicators, but outside of the mapped shear zone, smaller and less commonly occurring dextral, ductile shear zones are also observed (Section 3.2.1). In the Granite Lakes segment of the SCSZ in the southern part of the study area, the main strand of the ductile shear zone is ~1 km wide and deforms the Triassic Koip rocks and several 10's of meters into the TIC. In the Sawmill Canyon segment, the shear zone widens to ~1.5 km, where it deforms all Triassic and younger rocks west of Saddlebag Lake. In the Cascades Lake segment, dextral kinematic indicators generally define a ~1 km-wide shear zone, outside of which kinematic indicators of dextral shear are rare. The main strand is ~1 km for 5–10 km northward along the SCSZ, with subparallel, smaller strands intermittently present to the east (Cao, 2015).

3.1.2. Brittle fault zone

A complex fault network with strike-slip kinematic indicators crosscuts the structures that define the ductile shear zone (Fig. 2). Within the Cascades Lake, Sawmill Canyon, and Granite Lakes segments of the SCSZ, brittle faults define a 1–2 km wide fault zone. The Granite Lakes and Sawmill Canyon segments of the SCSZ cumulatively demonstrate a minimum of 1 km apparent dextral offset along brittle faults (Fig. 2). The duplication of the Triassic Koip mafic-intermediate metavolcanic rock unit is consistent with a minimum of 5 km offset (Unit Tr_a, Figs. 2 and 3), but folding subsequently obscured by faulting is also possible. The longest fault strands strike north-northwest and shorter faults branch from them, more commonly striking north to north-northeast. Two continuous fault strands that are parallel to and overprint the ductile shear zone are together continuous for the entire extent of the brittle fault zone in the Saddlebag Lake pendant. The northern strand is herein referred to as the Steelhead Lake fault, and the southern strand is referred to as the Maul Lake fault (MLF). These strands overlap along strike and are separated by ~200 m of rock in the Sawmill Canyon segment of the SCSZ (Fig. 4). Multiple NE striking faults are observed in and around the overlap zone, and more oblique faults (N-NW-striking) are truncated by both major fault strands (Fig. 2). The overlapping of these faults as well as the oblique faults between them are collectively interpreted as being part of a dilational jog, schematically illustrated in Fig. 5. A repeating, folded strike-slip duplex system is observed on the scale of the jog (Fig. 4).

3.2. Description of deformation structures

3.2.1. Ductile structures

Evidence for non-coaxial, ductile, dextral shearing in the SCSZ in the western Saddlebag Lake pendant is preserved by kinematic indicators involving metamorphic minerals, dikes, veins, and protolith clasts and crystals. Non-coaxial shear in the main shear zone and the smaller anastomosing dextral shear strands is defined by 1) asymmetric recrystallization of quartz (Fig. 6a); 2) asymmetric dextral kinematic indicators on subhorizontal surfaces that define the mapped shear zone, including asymmetric folding of bedding (Fig. 6b), asymmetric folding of quartz veins (Fig. 6c; Compton et al., 2017), asymmetric folding of other hydrothermal veins (Fig. 6d), asymmetric boudinage (Fig. 6e), and stretched, imbricated, sigmoid- and deltoid-shaped clasts (Fig. 6f).

The smaller dextral shear strands are separated by zones of dominantly coaxial shear accommodated by subvertical stretching indicated (illustrated in Fig. 5) by a steeply plunging penetrative stretching lineation. Evidence for concomitant coaxial and non-coaxial shear includes 1) felsic dikes and hydrothermal veins interpreted to be related to the late stages of TIC magmatism, which exhibit symmetrical and commonly isoclinal folding (Fig. 6g and h) and boudinage in outcrops that lack kinematic indications of dextral non-coaxial shear; 2) the metamorphic minerals that suggest growth or recrystallization at greenschist facies and lower conditions define both coaxial and non-coaxial foliations, which is consistent with both shear types occurring under similar or equal metamorphic conditions; 3) the Gem Lake segment of the SCSZ is 30 km south of the Sawmill Canyon along strike, they have overlapping cooling histories (Sharp et al., 2000; Paterson and Memeti, 2014). Coaxial and non-coaxial deformation occurred between 85 and 80 Ma in the Gem Lake segment (Sharp et al., 2000), indicating that these strain styles were similarly temporally coupled to the north in the Sawmill Canyon-Cascades Lake segments.

Rocks in the Saddlebag Lake pendant generally have a ubiquitous NNW-striking, steeply dipping foliation. Metamorphic foliations in the rocks within Fig. 2 on average strike 346 and dip 80° ENE (n = 127; following the right-hand rule), but many individual measurements also dip to the west (Fig. 7a). Mineral stretching lineations, have an average orientation of 116/77° (n = 34), and conform to a girdle of 350/79° (Fig. 7b). Metamorphic foliations formed by non-coaxial shear parallel the coaxially-formed metamorphic foliations. The average metamorphic foliation of dextral ductile shear planes has an orientation of 342/78° (Fig. 7c).

The Cathedral Peak unit of the TIC includes both magmatic and subsolidus dextral shear in the Cascades Lake segment of the SCSZ in the 20 Lakes Basin area (Fig. 3; Tikoff et al., 2005) and further north in the Virginia Canyon segment (Cao et al., 2015). Some of the shear zone may have been intruded by the TIC, based on highly sheared stoped blocks (Cao, 2015). The magmatic and high temperature, subsolidus, steeply dipping foliations and steeply plunging lineations of TIC rocks provide evidence that the same dextral, transpressive shear documented throughout the SCSZ was penecontemporaneous with this final major TIC phase cooling below the solidus around 85 Ma (Tikoff et al., 2005; Cao et al., 2015). The ~88-86 Ma Cathedral Peak phase of the TIC is correlated with multiple dikes that are ductilely deformed within the shear zone. The TIC includes stoped blocks deformed by subsolidus shearing, and preserves magmatic and subsolidus, steeply dipping foliations and steeply plunging lineation (e.g. Žák et al., 2007; Cao et al., 2015). Taken together, these observations indicate the shear zone was active syn-to post-intrusion of the TIC.

3.2.2. Transitional structures

The Sawmill Canyon segment of the SCSZ contains structures involving both ductile and brittle deformation. All folds measured within the map area have an average axis of 115/73° (n = 16; Fig. 7d), either measured directly or calculated using limb and hinge orientations. In folds with > 5 m half wavelengths (Fig. 4), flexural slip planes are

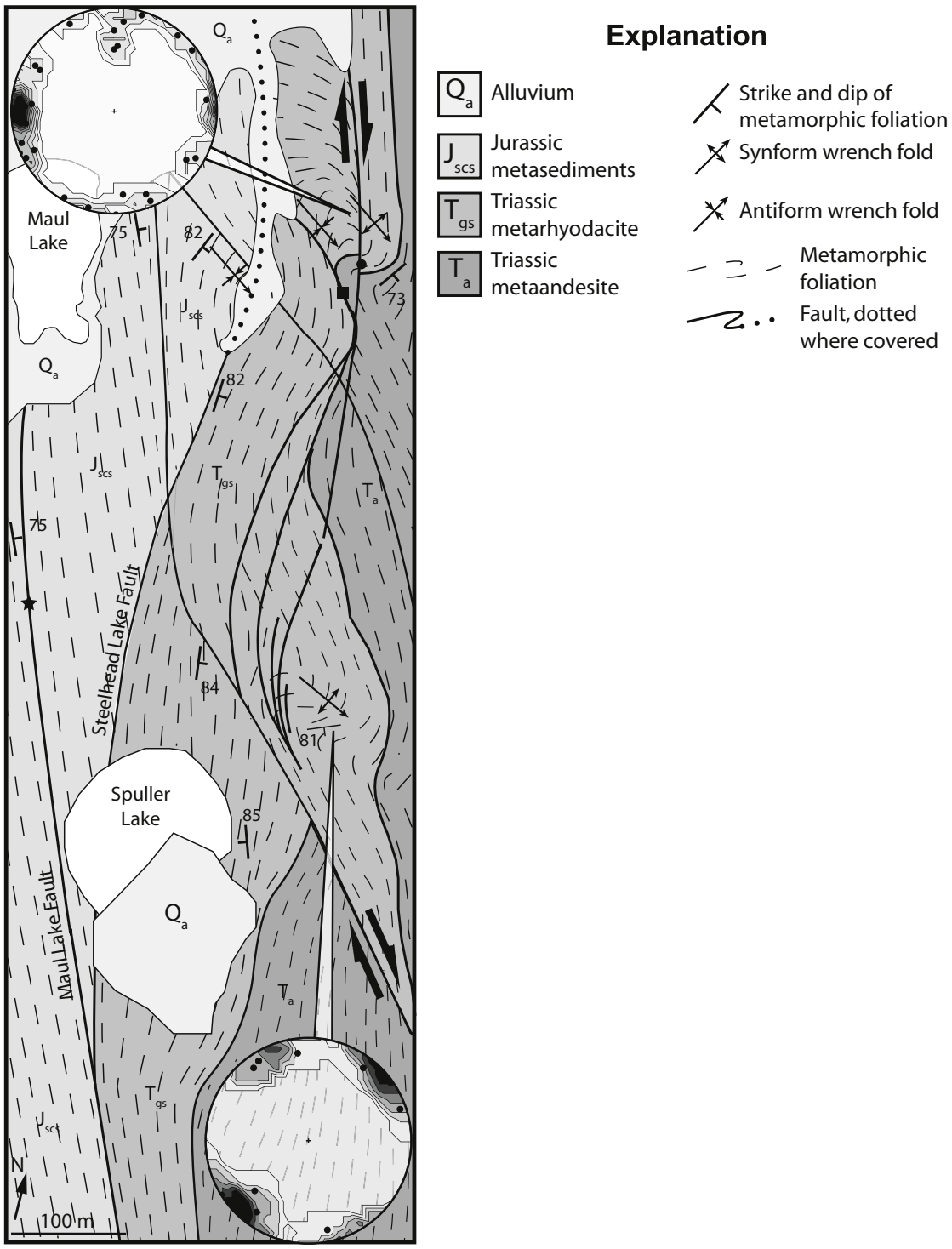

Fig. 4. Geologic map of the area from Sawmill Canyon to Spuller Lake. Triassic metavolcanic rocks are juxtaposed with Jurassic metasedimentary rocks by the Steelhead Lake fault. This fault curves into the Maul Lake Fault (MLF). Poles normal to the metamorphic foliation defining the northern fold have a girdle at 224/7 (n = 35), and the southern fold forms a girdle at 202/8 (n = 14). An imbricate fan overprints the southern fold with a shear plane striking southwest. These faults are sealed by m-scale quartz veins. The black circle in this map shows the location of Fig. 8c and f. The black square indicates the location of Fig. 6c and 8b, and sample SMC-13-5. The black start is on the MLF and shows the location of Fig. 8g (host rock/damage zone) and Fig. 12 (fault core).

defined by epidote-mineralized, subhorizontally lineated slip planes with a girdle of 020/10° (Figs. 7e and 8a). In the "northern fold" in Fig. 3, a brittle, brecciated, quartz-sealed fault (Fig. 8b), and the two Triassic metavolcanic rock units juxtaposed by it, are curved > 90°, and subparallel to the folded metamorphic foliation. A younger, steeply dipping brittle fault that locally strikes due north cuts and offsets this folded fault and rocks by ~20 m at the inflection point (Fig. 4). The quartz that seals this younger fault displays drag-folding in a dextral sense (Fig. 8c). This establishes a sequence defined by brittle faulting, followed by drag folding, younger brittle faulting, and younger drag folding. Additionally, two outcrops were observed with east-west striking, quartz- and tourmaline-sealed faults with sinistral drag folds in

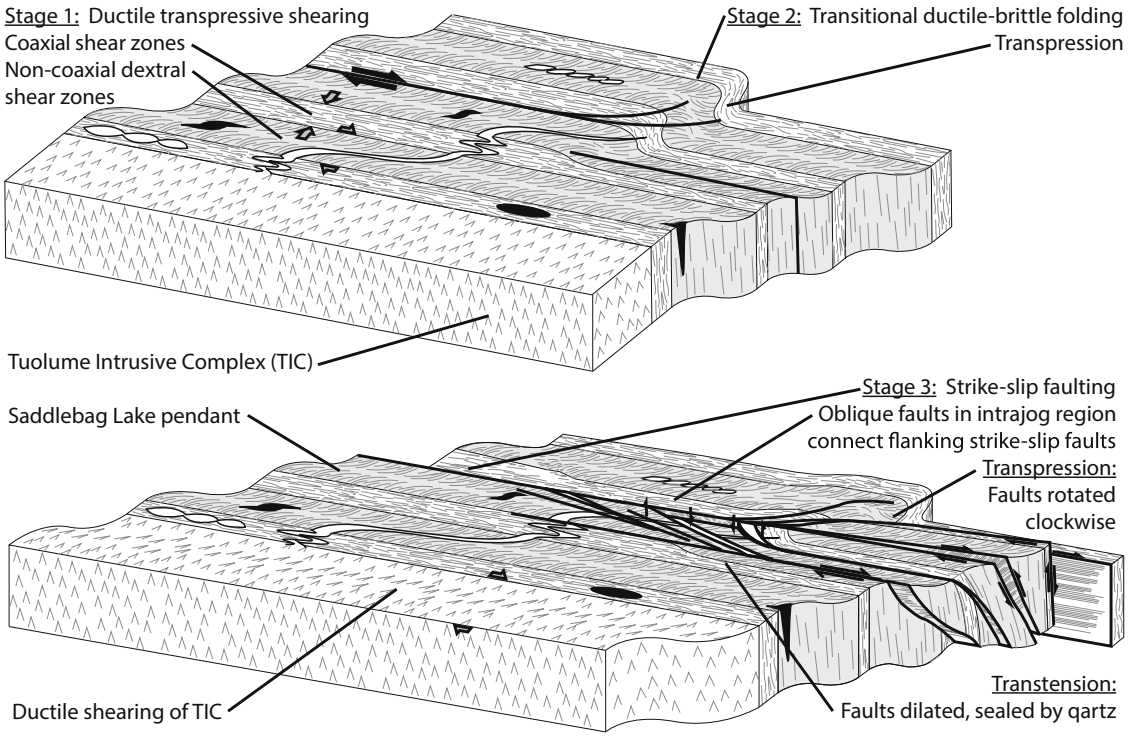

Fig. 5. Schematic illustration showing the interpretation of the structural evolution of the ductile, transitional, and brittle structures of the southern part of the western Saddlebag Lake pendant. Stage I began before intrusion of the TIC and continued afterwards. This stage involved ductile zones of both coaxial and dextral-sense non-coaxial shear at hot (amphibolite facies) conditions. Stage II involved the nascent stages of brittle faulting, along which ductile folds formed, accommodating some dextral offset (between amphibolite facies and brittle conditions). The TIC was deformed by hypersolidus and subsolidus dextral shear during and after emplacement in Stage I and into Stage II. Stage III involved the further development of the brittle fault zone, during which two main fault strands were linked by oblique faults that dilated, accommodating the flanking strike-slip faults. This dilation was kinematically transtensional. Earlier brittle faults rotated during Stages II and III were kinematically transpressive.

Triassic metavolcanic rocks in the Sawmill Canyon segment (Fig. 8d).

3.2.3. Brittle structures

Faults dip steeply, with an average of 348/84° (Fig. 7f), and are defined by offsets of stratigraphic units (Figs. 2–4), offsets along unmineralized, polished planes that contain slickenlines, hydrothermal veins with slickenlines, > 0.25 m quartz-sealed faults, fault breccias, cataclasites, and pseudotachylytes. Dextral offsets are inferred from the combination of apparent dextral offset of bedding and subhorizontal slickenlines (trend = 344, plunge = 5; Fig. 7g), the occurrence with dextral-sense drag folds, and outcrop-scale dilational jogs at right-steps (Fig. 9).

3.2.3.1. Slickenlines. Subhorizontal slickenlines are common on brittle fault planes in this area. They are defined by straight grooves in polished wall rock, in mineral cement along subvertical outcrop faces (Fig. 8e), and in quartz veins (Fig. 8f). Cement minerals include quartz, epidote, and tourmaline.

3.2.3.2. Quartz-sealed faults. Quartz-sealed fractures and faults are abundant in the Sawmill Canyon segment. They occur with a wide range of thicknesses from < 1 cm to > 10 m, have an average orientation of 349/89° (Fig. 7h). Quartz veins are most abundant and widest in the Sawmill Canyon segment of the SCSZ and become thinner and rarer to the north and south. There are dozens of > 0.25 m wide quartz veins observed in the Sawmill Canyon segment. The quartz veins commonly occur in multiple colors of quartz (Fig. 10a). Some thin magmatic dikes cross-cut thin quartz veins (Compton et al., 2017). We also found a ~0.25 m dike that cross-cuts a ~0.25 m quartz vein, but the dike is thinner and steps to the right where it cross-cuts the quartz vein (Fig. 10b). These field observations indicate an overlap in the timing of hydrothermal fluid flow and igneous activity. Fluid flow and quartz precipitation into outcrop-scale fault segments with right-steps, producing dilational jogs, are illustrated by the structure in Fig. 9.

Quartz veins have a wide range in grain size (10 μm to **1 mm**) and textures. Textures include bimodal grain size distributions that are aligned along simple planes or have more complicated patterns. Some quartz crystals are arranged as a vuggy texture (Fig. 8h), and some prismatic crystals display oscillatory growth zonation under a cathodoluminescent microscope (Fig. 11a). Another common quartz texture pattern is that fine-grained matrices fill the space between coarse, prismatic crystals (Fig. 11b), and in some cases grain sizes grade from coarse to fine (Fig. 11c). Other quartz textures include crack-seal/crustiform banding (Fig. 11d), jigsaw pattern (Fig. 11e), and plumose texture (Fig. 11f) with clearly higher fluid inclusion populations relative to the host grain on which the plumose structure was seeded (Fig. 11g). Brittle deformation textures in veins include slickenlines and angular to rounded host rock or older vein clasts in breccia and cataclasite. Grain boundaries are commonly straight and, at triple junctions commonly form at around 120°, overprinting earlier quartz vein textures.

The most well exposed example of the quartz-sealed faults in the Sawmill Canyon segment is the Maul Lake fault (MLF). The grid map in Fig. 9 shows part of the > 10 m wide composite quartz vein that comprises part of the northern segment of the MLF (location shown by star in Fig. 4). This wide quartz vein is the northernmost recognized exposure of the MLF, and is at least ~5 m wide for about 300 m along strike between Maul and Spuller Lakes. The outcrop in Fig. 12a (northern MLF) is defined by four main quartz domains that are each several meters wide. The outer east and west domains are gray to white, and the two inside domains are green and blue (Fig. 12b). All domains are cut by thin white veins, which also extend into the host rock and

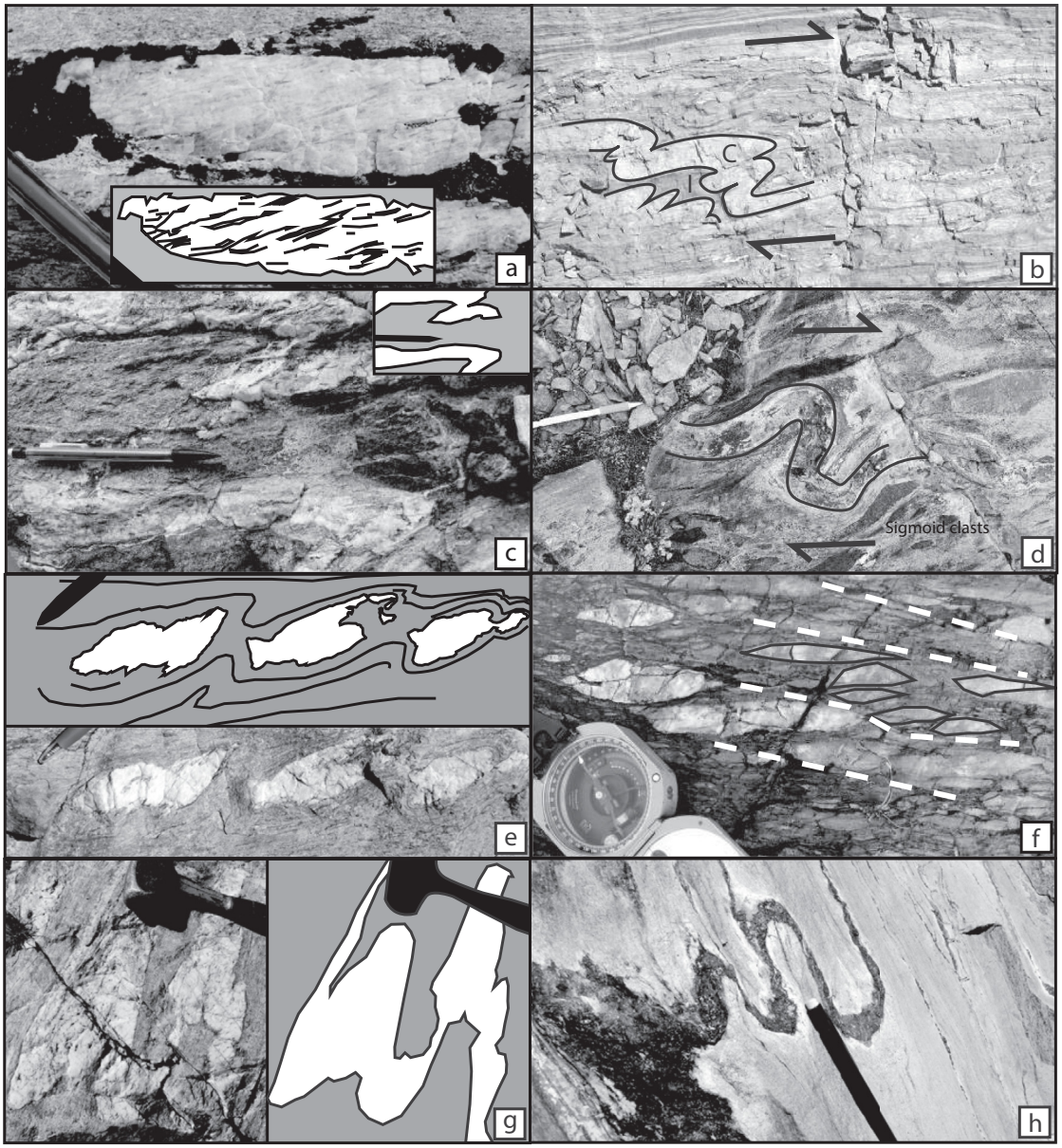

Fig. 6. Field structures demonstrating ductile deformation. a) quartz vein with elongate grain boundaries aligned in a dextral sense, b) folding of competent (c) and incompetent (i) sedimentary layers in the metamorphosed calc-silicate rocks, c) asymmetrically folded quartz veins, folded in a dextral sense, and illustrated with a sketch, d) asymmetrically folded epidote vein in a dextral sense, e) asymmetric (dextral-sense) boudinage, with metamorphic foliation locally wrapping the boudines but aligned parallel and straight away from the boudines, f) conglomerate clasts showing ductile dextral sense of shear, g) symmetrically folded TIC-related dike, h) symmetrically folded tourmaline vein with leach zones in the host rock.

form a quartz-sealed fracture mesh (Fig. 8g). The thin white veins in the western and blue quartz domains are truncated by the green domain, which is itself cross-cut by thin white domains. These cross-cutting relationships indicate that the formation of the domains and the thin white veins overlapped in time, and thus represent multiple discrete fracturing and vein formation events. South of Spuller Lake, the fault maintains similar dimensions, but breccias and cataclasites comprise most of its contents, in addition to quartz veins and pseudotachylytes (Sections 3.2.3.3 to 3.2.3.5).

3.2.3.3. Breccia. Breccias are present in many of the brittle faults in this system and contain millimeter-to centimeter-sized angular fragments of the local wall rock in a matrix of extremely fine-grained quartz, epidote or tourmaline (Fig. 13a and b). They occur at both left and right steps of about a centimeter to a meter in the traces of faults with apparent dextral offset, and also form tabular bands tens of centimeters thick that extend for meters along strike. In quartz-sealed faults, fault breccias (breccias with displaced rigid clasts due to displacement of fault walls) and cataclasites contain quartz matrices surrounding angular quartz clasts (up to 0.2 mm) with random orientations. Other breccias are interpreted as fluid-driven, and are those with clasts separated only by hydrothermal mineral veins and that lack evidence of significant rigid body displacement or rotation relative to surrounding clasts or fault wall. The MLF, south of the wide quartz vein (south of Spuller Lake), is defined by a ~5 m wide zone of breccia, cataclasite, ultracataclasite, all of which were cemented by quartz, tourmaline, illite, or epidote.

3.2.3.4. Cataclasite and ultracataclasite. Cataclasites are generally composed of angular to rounded fragments in a matrix containing

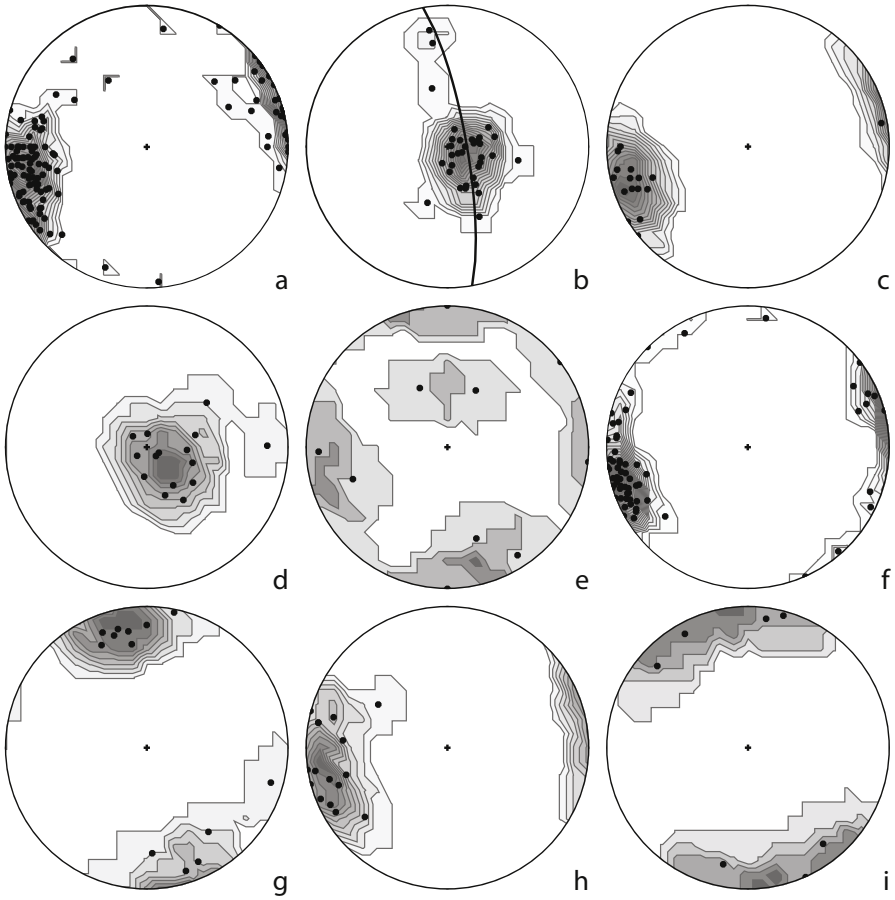

Fig. 7. Equal area lower hemisphere stereonet projections of structures in Sawmill Canyon with Kamb contours (C.I. = 1σ). 'Poles to planes' are poles that are orthogonal to measured plane orientations, and lineation poles are parallel to measured lineations. Projections calculated and plotted with the program OSXStereonet (Cardozo and Allmendinger, 2013). a) Poles to planes of metamorphic foliations. The average plane is 346/80 (n = 127). b) Poles parallel to metamorphic stretching lineations. The average orientation is 116/77 (n = 34). c) Poles to planes of metamorphic foliation of dextrally sheared rocks. The average plane orientation is 342/78 (n = 16). d) Poles parallel to axes of folds, calculated from plane orientations. The average pole orientation is 115/73 (n = 15). e) Poles parallel to lineations in epidote-rich flexural slip planes within folds. The average pole is 198/10 (n = 10). f) Poles to planes of brittle faults. The average plane is 348/84 (n = 65). g) Poles to planes of quartz veins. The average plane orientation is 352/76 (n = 16). h) Poles parallel to slicken lines. The average pole is 344/5 (n = 13). i) Poles to planes of sinistral faults. The average plane is 164/85 (n = 13).

smaller angular grains (Fig. 13c and d). Many cataclasites also contain epidote, chlorite and quartz cementation in greater abundances than the surrounding rock. Cataclasites contain a combination of fragments of wall rock and fragments of the hydrothermal phases. Cataclasites form continuous bands from centimeters-to tens of centimeters-thick, subparallel to the fault. The edges of these bands commonly display slickenlines and other kinematic criteria such as crescent marking or crystal fibers (e.g. Doblas, 1998). Ultracataclasites occur in extremely fine-grained dark grey to greenish-black bands that locally crosscut adjacent cataclasites along sharp boundaries. They contain millimeter to sub-millimeter rounded clasts of quartz and feldspar (which is often sericitized). Quartz clasts contain evidence of subgrain formation due to dynamic recrystallization of quartz prior to the formation of the cataclasite. Aligned long axes of clasts define a weak grain shape fabric at the grain scale. Some ultracataclasite clasts are composed of epidote or quartz. The groundmass between clasts is predominantly angular epidote and quartz at all scales of observation to tens of micrometers.

3.2.3.5. Pseudotachylyte. Pseudotachylytes are present in branching faults adjacent to the main fault strands, and as veins crosscutting some of the fault rocks within the main fault strands. Small offset fault veins are purple to pinkish-grey and range in thickness from < 1 mm to ~15 mm. They are planar, aphanitic, contain few pale-colored clasts, and are color-banded with bands parallel to the edges of the veins. Injection veins of the same aphanitic purple material branch from the fault veins at high angles (Fig. 13e) and contain color-banding parallel to their edges. Lath-shaped, felsic microlites up to 10 μm are aligned in some bands but non-aligned in others (Fig. 13f). Rounded lithic fragments and quench textures occur in isotropic matrices (Fig. 13f). Spherulitic overgrowths around lithic fragments are present in some of the compositional bands. Micrometer scale, round inclusions of bright minerals in back scattered electron scanning electron microscope images (Fig. 13f) and black and opaque in plane polarized light (Fig. 14) are likely metal oxide droplets. The pseudotachylytes crosscut epidote-rich cataclasites, in some cases with gradational boundaries (Section 5.4). Injection veins are ductilely sheared in adjacent fault rock. A micro-scale map was made of pseudotachylyte sample G3 (Fig. 14) from the MLF in a zone of breccia and cataclasite. Quartz clasts from the protolith are entrained in the pseudotachylyte matrix and are commonly rounded. The clasts are commonly < 0.5 mm, but range up to 3 mm. Microfaults offset all materials by 1–2 mm, and are sealed by younger quartz veins.

3.2.3.6. Sinistral faults. Northwest-striking, highly oblique faults are also observed. Where offset is observable, these faults are all sinistral and antithetic to the main brittle fault zone. Sinistral faults have an average of 075/89° (n = 7, Fig. 7i). Offsets are all on the order of 1–10 cm and are all the youngest deformation feature where observed.

4. Stable isotopes

4.1. Oxygen isotope geochemistry of quartz veins

4.1.1. Methods

The quartz $\delta^{18}O$ values for composite veins, fault breccias (matrix and clast), and cataclasites (matrix-clast mix) were determined for samples from brittle fault zones up to 12 km north and 13 km south of Sawmill Canyon (Fig. 15). The $^{18}O/^{16}O$ isotope ratios were determined at IIRMES, California State University, Long Beach. Quartz samples were cut, unweathered parts were separated and crushed, and grains were loaded to ~2–3 mg. Oxygen was liberated from quartz by a

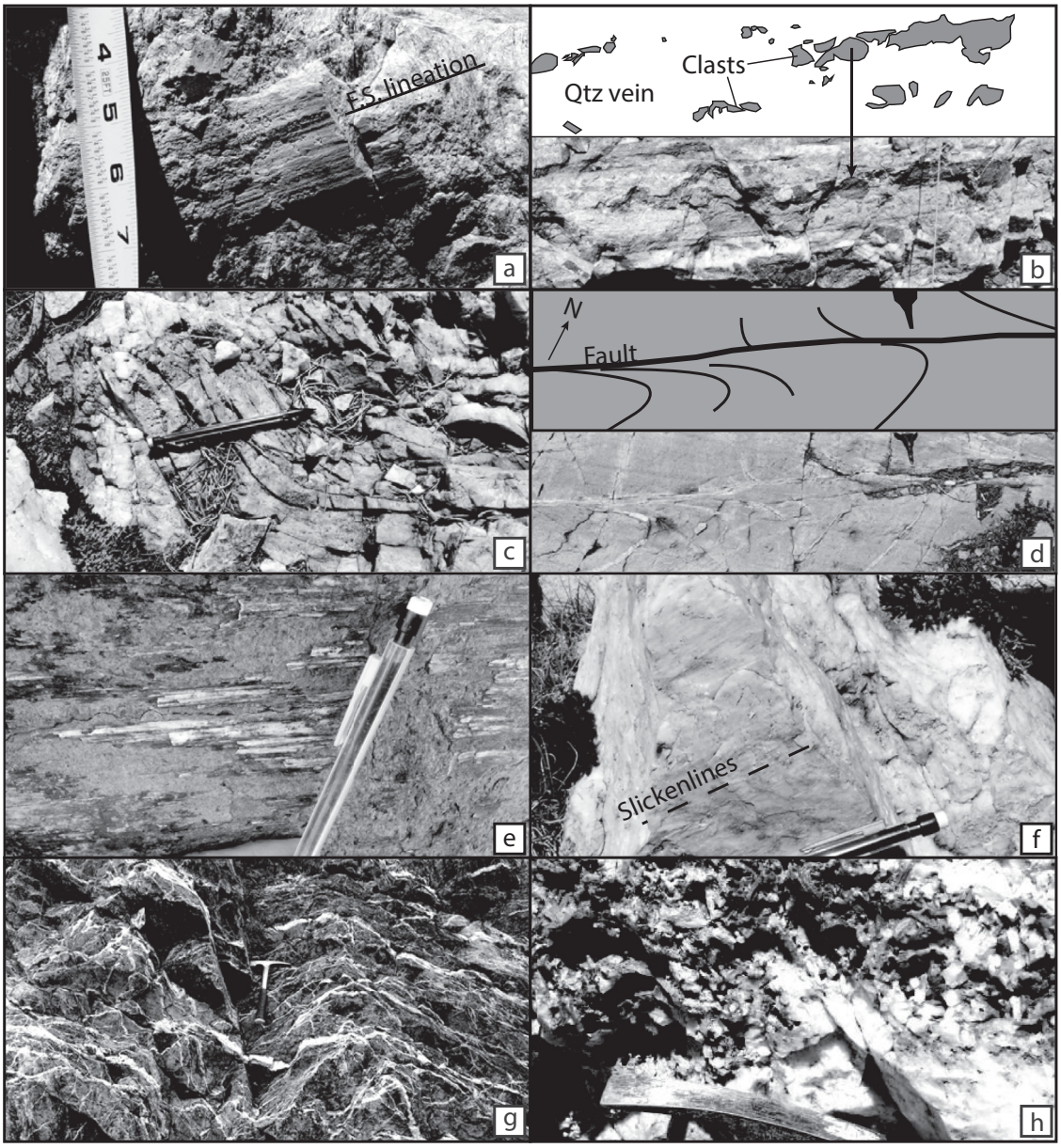

Fig. 8. Brittle-ductile and brittle field structures demonstrating mineralization during deformation. a) Epidote mineralized flexural slip lineations parallel to folded metamorphic foliation, b) quartz-sealed fault breccia within a fault, c) drag-folded quartz vein, d) sinistral fault with sinistral-sense drag folding, mineralization includes quartz and tourmaline, e) quartz-mineralized subhorizontal slickenlines, f) slickenlines on a quartz vein, g) quartz veins in the house rock west of the Maul Lake Fault outcrop in Fig. 12, h) vuggy quartz.

modified version of the laser fluorination method from Sharp (1990) that eliminates the conversion to CO_2. Oxygen (O_2) was then transferred to the ThermoFinnigan DeltaPlusXP light-isotope-ratio mass spectrometer for determination of $\delta^{18}O$ values. Oxygen isotope ratios are reported in delta notation relative to V-SMOW ($\delta^{18}O_{NBS-28}$ = 9.6‰). Replicate samples of the Caltech rose quartz working standard ($\delta^{18}O$ = 8.45‰) produce analytical error of ± 0.2‰.

4.1.2. Results

The $\delta^{18}O$ values range from 14.5 to −3.2‰ (n = 79; Table 1, Fig. 15). Lowest values occur in the jog zone (both the main flanking fault strands and the smaller faults) in the Sawmill Canyon segment of the SCSZ. Values < 1‰ were only observed in veins from Sawmill Canyon to Granite Lakes, a distance of ~4 km. Quartz $\delta^{18}O$ values from > 1 km north of Sawmill Canyon do not fall below 9‰ and range from 14.5 to 9.3‰ (n = 5). About 4 km south of Sawmill Canyon, the MLF juxtaposes Jurassic Koip sequence metavolcanic rocks with the TIC; a quartz vein that seals the fault next to Granite Lakes (Fig. 2) has a $\delta^{18}O$ value of 0.8‰. Most of the area south of Granite Lakes is covered by Quaternary alluvium, covering any veins that are present. South of Granite Lakes, the few quartz vein samples have $\delta^{18}O$ values > 12.5‰ (n = 5). The Sawmill Canyon to Granite Lakes segment has $\delta^{18}O$ values that span the full range recorded during this study (−3.2–14.5‰; n = 69).

Vein quartz $\delta^{18}O$ values for quartz from the MLF range from 11.4 to −1.5‰ (n = 40). The highest values are seen in the eastern quartz domain, the intermediate values are from the western and blue quartz domain, and the lightest values are from the green quartz domain (Fig. 12b). The relative timing of the domains inferred above based on cross-cutting relationships consequently indicates a correlation between decreasing $\delta^{18}O$ values and decreasing age (Fig. 12b and c). No such obvious pattern is revealed in the $\delta^{18}O$ values of the thinner (cm-

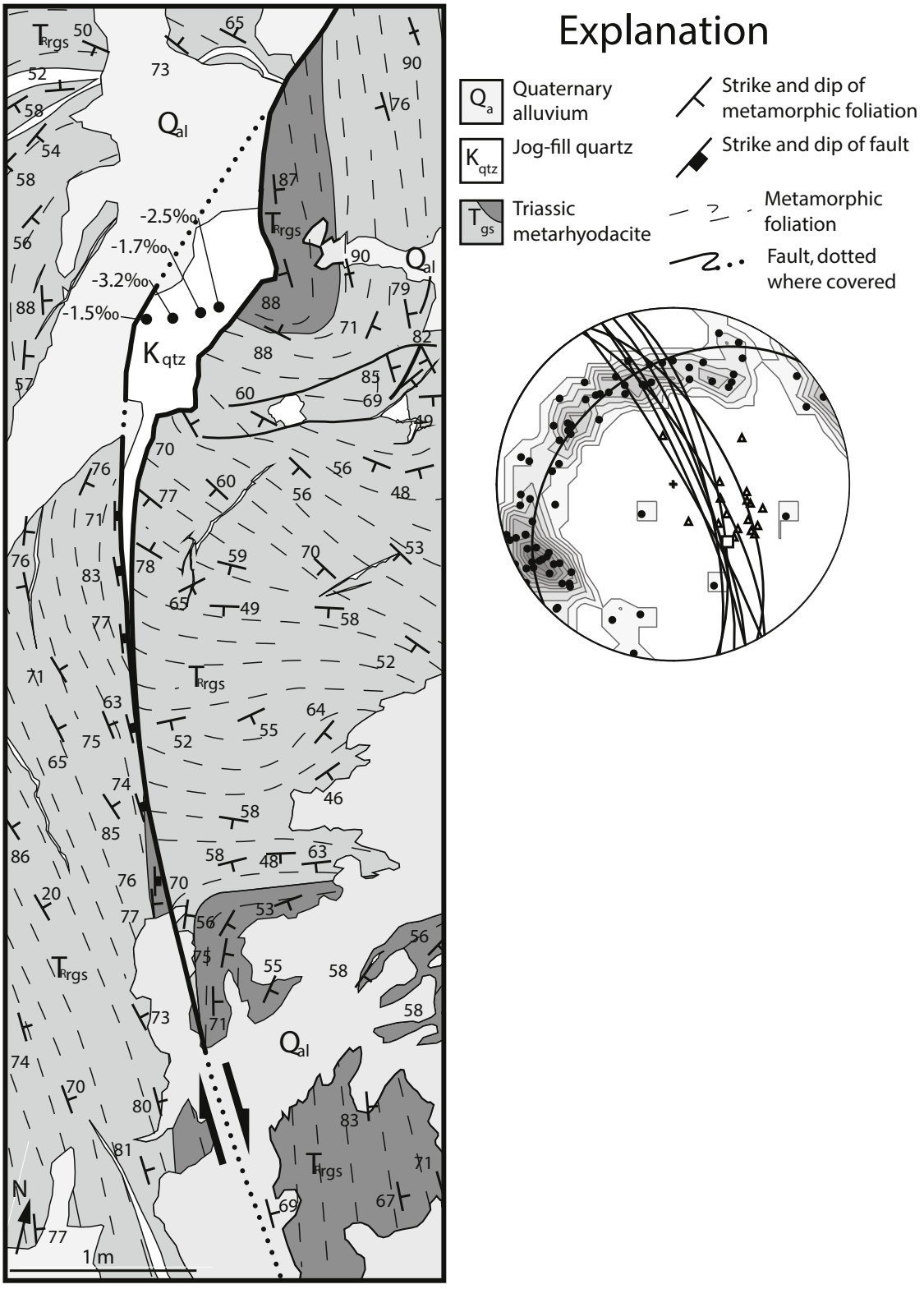

Fig. 9. Grid map of a fold in the youngest Triassic Koip metarhyolite defined by metamorphic foliation and older quartz veins. The 'z' shape of the fold orientation indicates dextral wrench rotation. The fold is offset in a dextral sense by a fault that intersects the inverted fold limb. A right-step in the fault produced a jog that was filled by quartz due to dilation. The dextral fault offset is indicated by the apparent offset of lithology near the bottom of the photo. The numbers represent the $\delta^{18}O$ (‰) values of four samples from across the jog quartz are shown in box bubbles. The stereonet shows poles to planes of metamorphic foliation (227/37, n = 76, black circles are poles to planes, the white square is the calculated fold axis), great circles representing the fault orientations (337/76, n = 8), and metamorphic stretching lineations defined by micas and stretched quartz (110/59, n = 17, white triangles). Location of map is shown by the black square in Fig. 2.

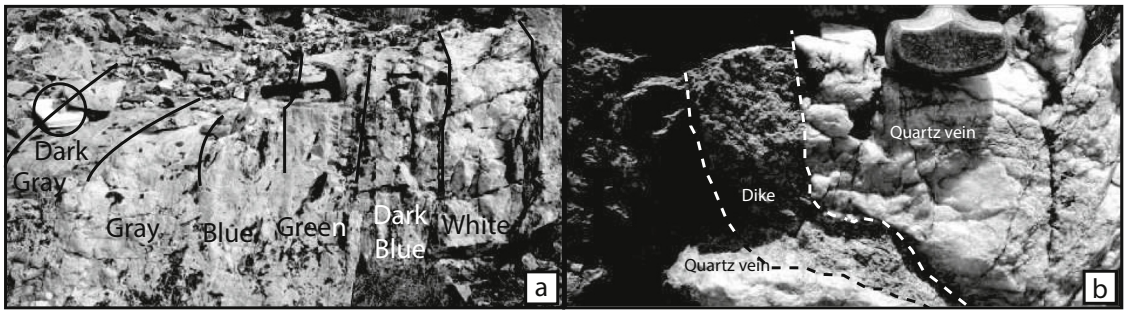

Fig. 10. Field photographs of quartz veins. a) Composite quartz vein-sealed fault with multiple colors of quartz veins, b) TIC-related dike cross-cutting a quartz vein.

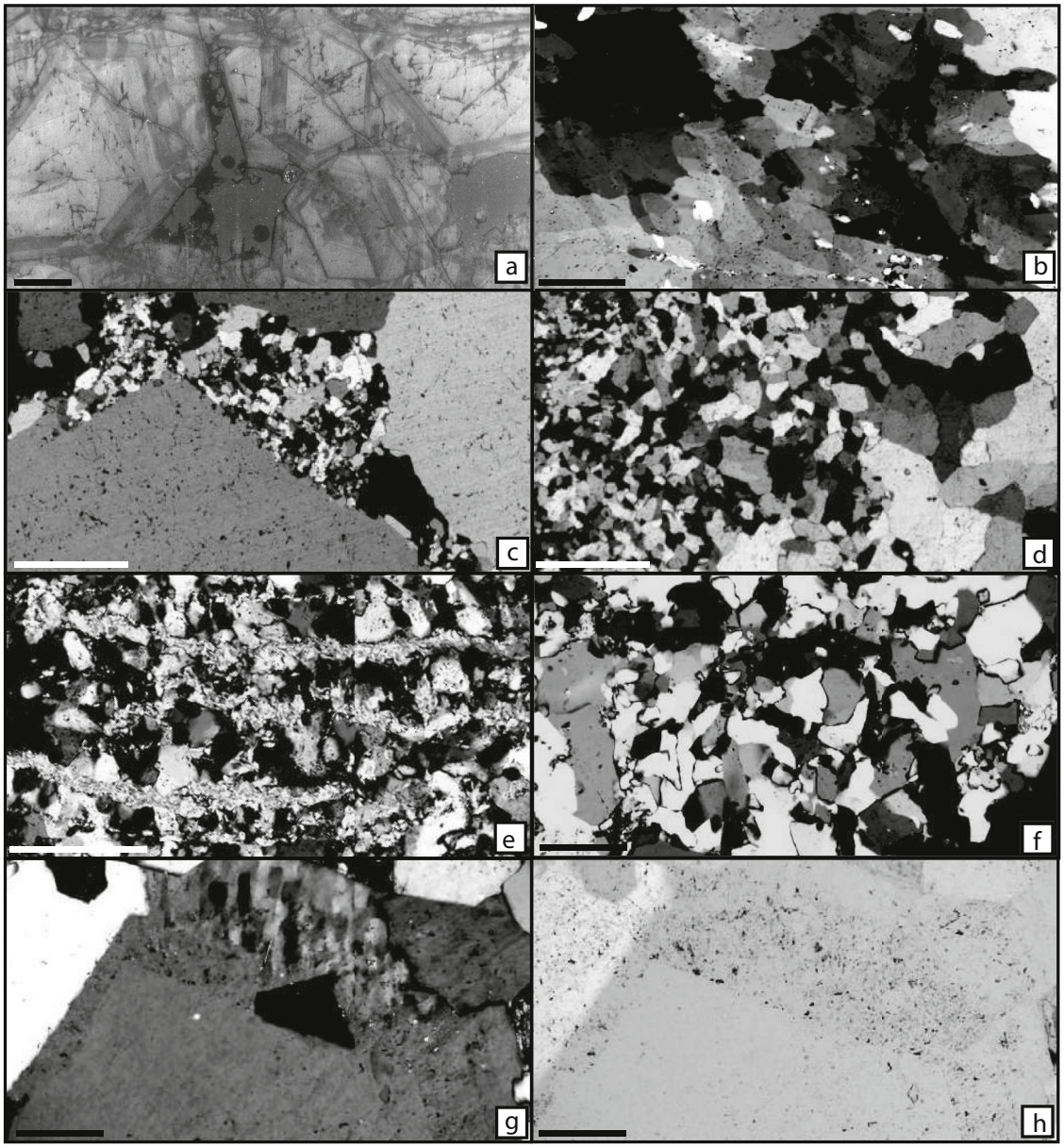

Fig. 11. Photomicrographs of quartz veins in cross-polarized light (except Fig. 11a). a) EBSD image of prismatic quartz crystals from a quartz vein, showing oscillatory zoning (scale = 1 mm), b) aligned quartz subgrains, grouped together with similar extinction magnitudes, indicating shared origin from larger grains (scale = 1 mm), c) prismatic quartz crystals and a matrix of fine-grained crystals pervading the space between the coarse crystals (scale = 1 mm). d) Gradient from fine to coarse (left to right) quartz crystals, which commonly have triple junctions near 120° (scale = 1 mm). e) Crustiform/crack-seal banding in quartz, with some layers delineated by illite (scale = 0.2 mm). f) Jigsaw pattern in quartz (scale = 0.2 mm). g) Plumose structure in quartz growing from a coarse, prismatic quartz crystal (scale = 0.2 mm). h) Same sample as Fig. 11g, but in plane-polarized light, showing high density of fluid inclusions in plumose structure relative to the prismatic quartz crystal on which the plumose quartz is coated (scale = 0.2 mm).

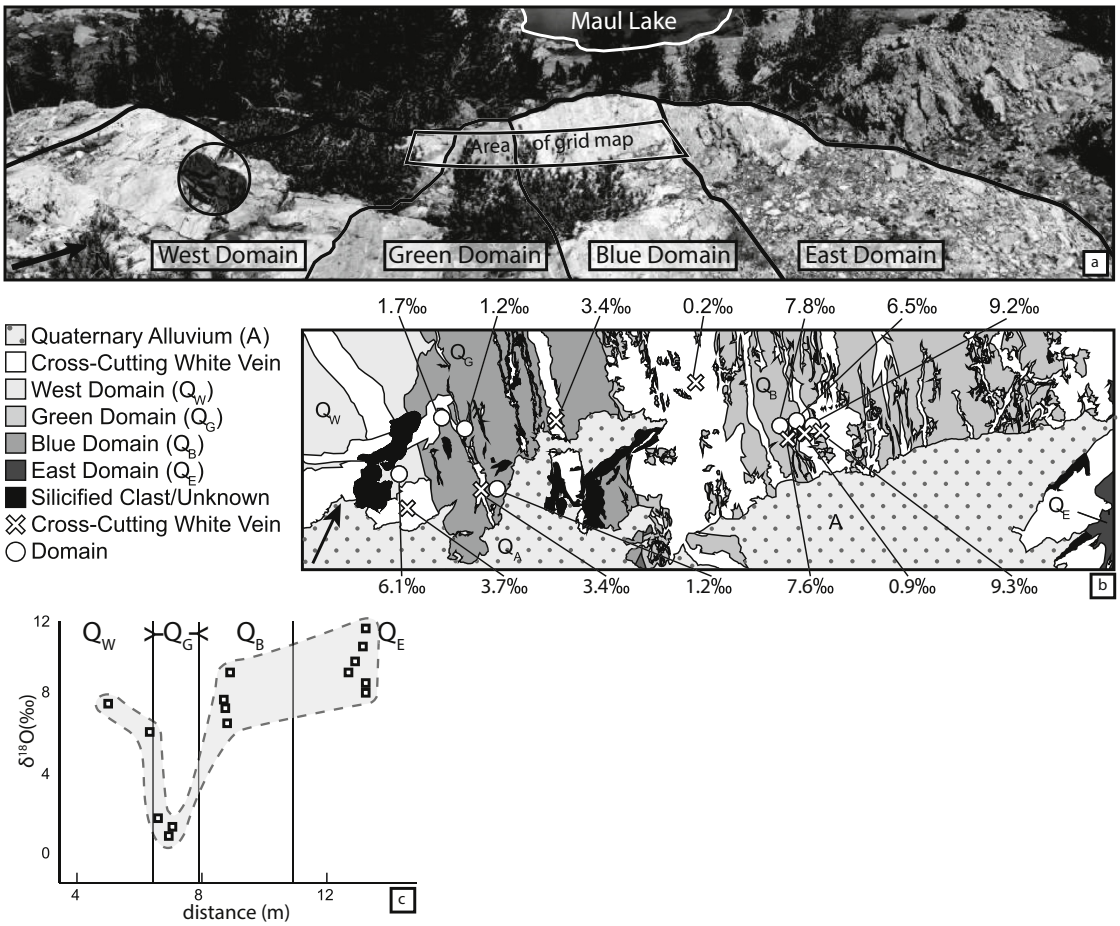

Fig. 12. a) photograph and b) grid map of an 11.5 m-wide episodically cracked and mineral-healed quartz vein segment of the MLF (location shown in Fig. 4). The fault is sealed by four several-meter-wide quartz domains recognized by color and $\delta^{18}O$ value (‰) range (from west to east, the domains are white, green, blue, and white, respectively). White quartz veins cut the domains. The green quartz domain cross-cuts white veins that cross-cut the west and blue quartz domain, and younger white veins cross-cut the green quartz domain. These cross-cutting relationships indicate that the formations of the two vein set types overlapped in time. This outcrop exposes the widest part of the quartz-sealed fault observed. The $\delta^{18}O$ values of quartz and their respective sample locations are shown. Fig. 12c shows the $\delta^{18}O$ values for quartz domains younging inward (indicated by the Y symbols) toward the green domain. A backpack (circled) is included in the photograph for scale.

scale) white cross-cutting veins.

The $\delta^{18}O$ values for additional quartz-sealed faults in the Sawmill Canyon segment were studied in detail (Fig. 4, and including samples from the outcrops shown in Figs. 6a, 8b and 9, 12 and 14). A complicated brittle, quartz-sealed fault (sample series SMC-13-5, part of the "northern fold" in Fig. 4, and shown in Fig. 8b) that contains fault breccia has $\delta^{18}O$ values that range from 12.1 to 4.1‰. A four-sample transect across a quartz-filled jog (sample series SMC-14-18, locations shown in grid map in Fig. 9) produced $\delta^{18}O$ values that ranged from −3.2 to −1.4‰. A five sample transect across a ~0.25 m-thick vein with vuggy quartz in the center (SMC-14-9) reveal high and homogeneous $\delta^{18}O$ values (9.0–9.5‰; n = 3) for the outer vein and lower values in the inner vein (5.6 and 5.3‰; n = 2), and prismatic vuggy quartz in the vein center has $\delta^{18}O$ = 4.0‰.

4.2. Pseudotachylyte

4.2.1. Methods

The $\delta^{18}O$ values of the pseudotachylyte sample G3 shown in Fig. 14, were determined with Secondary Ion mass spectrometry (SIMS) at University of California, Los Angeles. The sample was cut into a thin section that was then was coated in gold and analyzed using a Cs^+ primary ion beam. Analyses were corrected using NBS612 glass standard (10.33‰).

The δ^2H values of this pseudotachylyte sample (G3) were also analyzed. Grains were wrapped in silver foil and baked at 150 °C overnight to remove adsorbed atmospheric vapor. Hydrogen was volatilized in a Thermocombustion elemental analyzer and transferred to the ThermoFinnegan MAT DeltaPlus-XP light-isotope-ratio mass spectrometer at the David W. and Claire B. Oxtoby Environmental Isotope laboratory at Pomona College, Pomona, California. Duplicate samples, with a target hydrogen signal of 15,000 mV, were analyzed in succession and results were normalized to the NBS-30 biotite standard (δ^2H = −65.7‰). The hydrogen isotope ratio is reported in delta notation relative to Vienna Standard Mean Ocean Water (V-SMOW). Analytical uncertainty is 2‰ (Table 1 in Fig. 15).

4.2.2. Results

The three phases analyzed in the sample were protolith quartz (both as the bounding host rock and as rounded survivor clasts), pseudotachylyte matrix, and younger quartz veins in microfaults that offset the pseudotachylyte vein margins. Pseudotachylyte matrix (n = 13), quartz clasts (n = 11), and cross-cutting quartz veins (n = 6) have average $\delta^{18}O$ values (1σ) of 3.3 ± 0.6‰, 12.6 ± 0.4‰, and 4.1 ± 0.1‰, respectively (Table 2). Two grains of the pseudotachylyte matrix from the same sample (G3) have δ^2H values of −135 and −138‰.

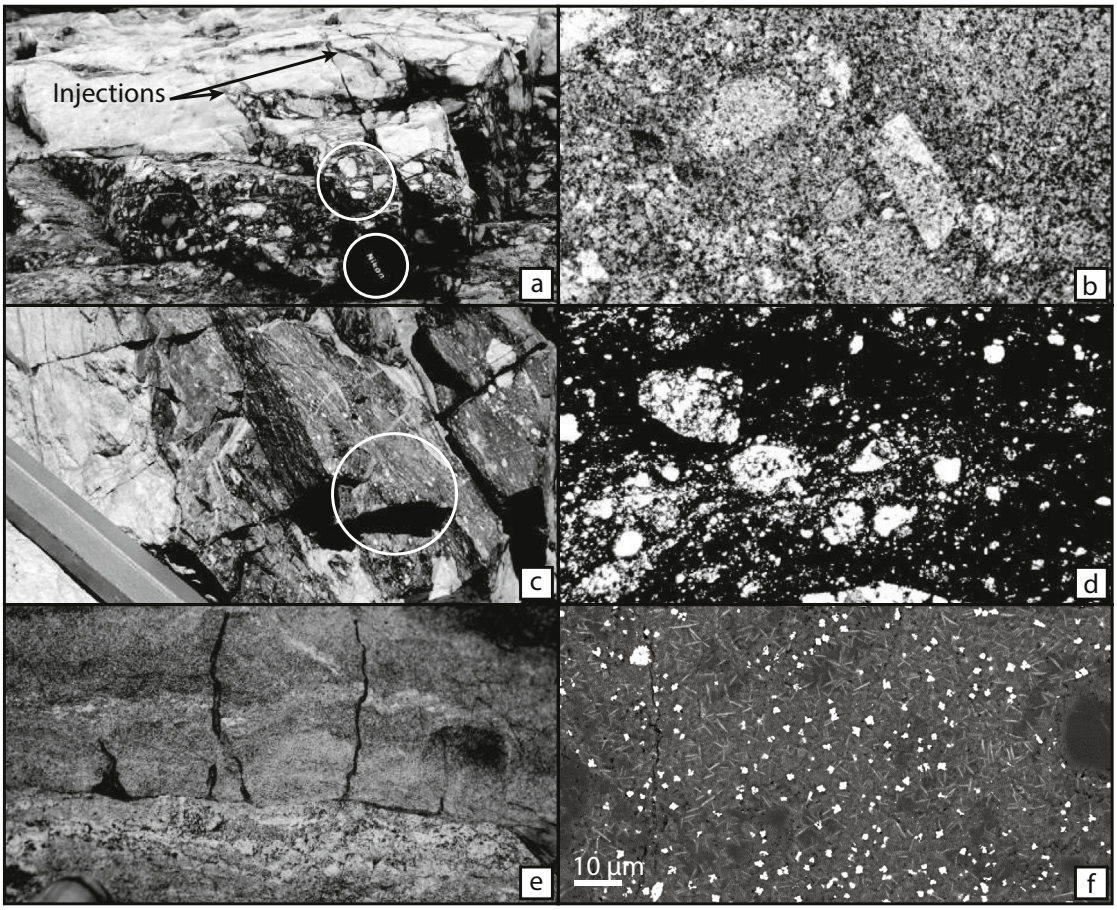

Fig. 13. Brittle deformation fabrics. a) Field photograph of quartz breccia clasts in a dark blue quartz matrix, with thin section shown in Fig. 13b. The clasts include angular quartz fragments and the matrix consists of fine-grained quartz (5 mm across). c) Field photograph of ultracataclasite with irregular orientations and rotated clasts suspended in matrix principally composed of tourmaline deposits, with thin section shown in Fig. 13d showing rounded quartz clasts in a fine-grained matrix (5 mm across). e) Field photograph of black vein showing structures indicative of pseudotachylyte injection at a high angle to the main plane of the vein. h) EBSD image of quench texture in the pseudotachylyte. The thin grains are interpreted as lathes and the equant (white) shapes are interpreted as metal oxides.

5. Discussion

5.1. Fluids in the Saddlebag pendant and TIC

The spatial distribution of $\delta^{18}O$ values for quartz veins in the Saddlebag Lake and Northern Ritter Range pendants suggests that during the syn-to post-intrusion transition from ductile to brittle deformation, meteoric-hydrothermal fluids were focused into the Sawmill Canyon/Granite Lakes segments (Fig. 15). Quartz veins precipitated from an aqueous fluid along faults with apertures that may have been up to or exceeding several mm, as evidenced by vuggy quartz. The earlier shear zone and later fault zone controlled the geometry of fluid flow, while the cooling TIC provided the energy for fluid flow along steep thermal gradients (Norton, 1984) on the scale of its contact with the SCSZ. Recrystallized quartz veins with low meteoric values are included in this several km^2 zone of quartz with low $\delta^{18}O$ values (Compton et al., 2017), demonstrating that incursion of meteoric-hydrothermal fluids was at least partly coincident with deformation at metamorphic conditions that permitted recrystallization of quartz veins.

The spread of $\delta^{18}O$ values represents an evolution of the fluids from which the quartz veins precipitated. An outcrop of the MLF contains quartz veins with cross-cutting relationships that demonstrate relative timing by truncation of outer veins by inner veins, the youngest being the white veins the cross-cut the green quartz domain in (Fig. 12b). The $\delta^{18}O$ values of the four main quartz domains in Fig. 12b decrease with decreasing relative age (Fig. 12c). We consider two hypotheses to explain this younging trend, both of which involve a meteoric-hydrothermal fluid source, because no other natural fluid would produce quartz veins with $\delta^{18}O$ as low as $-3.2‰$.

One hypothesis is that the quartz precipitated from a single fluid source that cooled over time, the quartz precipitating from the cooler fluid having elevated $\delta^{18}O$ values due to higher equilibrium quartz-H_2O fractionation factors. Because cross-cutting relationships indicate that quartz $\delta^{18}O$ values decreased over time, this model would require that the meteoric-hydrothermal fluid source started out coolest and continually heated, in contrast to the cooling pattern of the rocks (e.g. Cao et al., 2016). This hypothesis also requires that the dilational jog is the oldest structure of the fault zone, and that over time, the fluids became less focused. Finally, it would require that the plastically recrystallized quartz veins with the highest $\delta^{18}O$ values of Compton et al. (2017) are the youngest veins, postdating veins with lower $\delta^{18}O$ values, brittle fabrics, and lacking evidence of plastic recrystallization.

The second hypothesis is that the spread of quartz $\delta^{18}O$ values represents a mixing trend between magmatic fluids produced by devolatilization of the TIC and younger meteoric-hydrothermal fluids. In this case, the veins with the lowest quartz $\delta^{18}O$ values would be the youngest. Compton et al. (2017) interpreted the source of earlier fluids from which hydrothermal quartz veins precipitated to be magmatic as opposed to metamorphic fluids because they were in isotopic equilibrium with tourmaline, which is abundant in late TIC dikes. Magmatism must have overlapped at least slightly with hydrothermal fluid

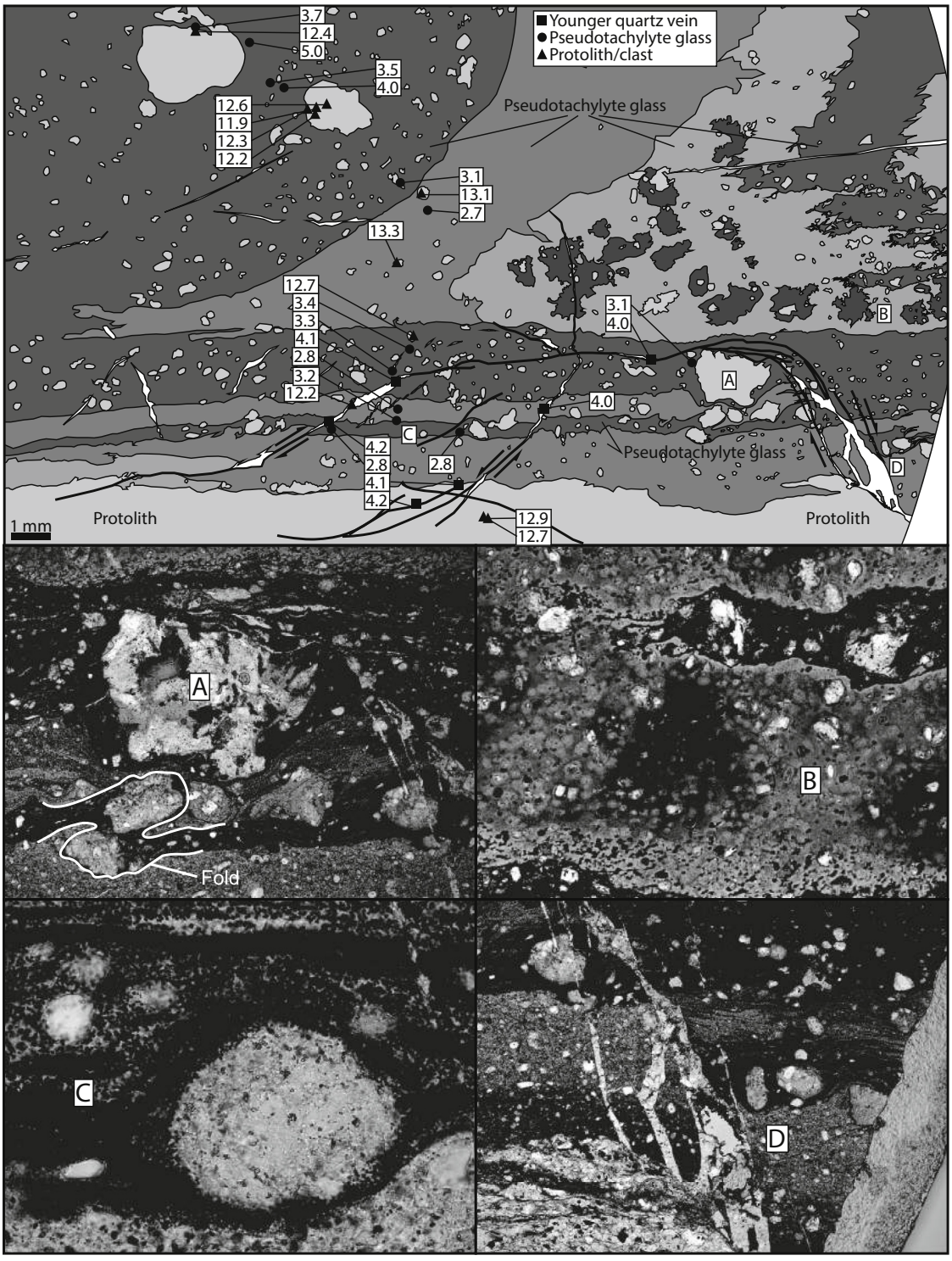

Fig. 14. Micro-scale map of a pseudotachylyte sample in thin section, and photomicrographs corresponding to four locations (A through D) in the map. The numbers in the boxes correspond to $\delta^{18}O$ values (‰). The bottom layer of the map is the protolith, and the same-colored grains are interpreted to be clasts of the protolith (eg. location A). Clasts also help to delineate tight microfolds, as seen in the first photomicrograph. Darker material is all interpreted to be pseudotachylyte glass. Flow bands are separated by compositional zonation. The map displays a flow-related fold. Islands of dark melt patch delineated by nebulous boundaries and often including protolith clasts that are coarser than clasts in the surrounding glass (eg. location B). The darkest glass is defined by alignment of equigranular opaques (eg. location C). The white material is quartz vein. In the bottom of the map, a microfault offsets all other components of the rock in a counter-clockwise direction, and the fault is sealed by quartz (eg. location D). Location shown by black star in Fig. 2.

flow. We observed a dike in Sawmill Canyon that cross-cuts a quartz vein (Fig. 10b). We interpret this dike to be a Cathedral Peak-phase dike, but another potential melt source is in situ or in source anatectic leucosome from partial melting of the pendant along its contact with the TIC (Albertz, 2006). Thinner (mm-to a few cm-scale) hydrothermal quartz veins were cross-cut by (mm-to a few cm-scale) dikes (Compton et al., 2017). Additionally, both dikes and hydrothermal veins are folded (Fig. 6c, d, g, h). In contrast, the Steelhead Lake fault truncates

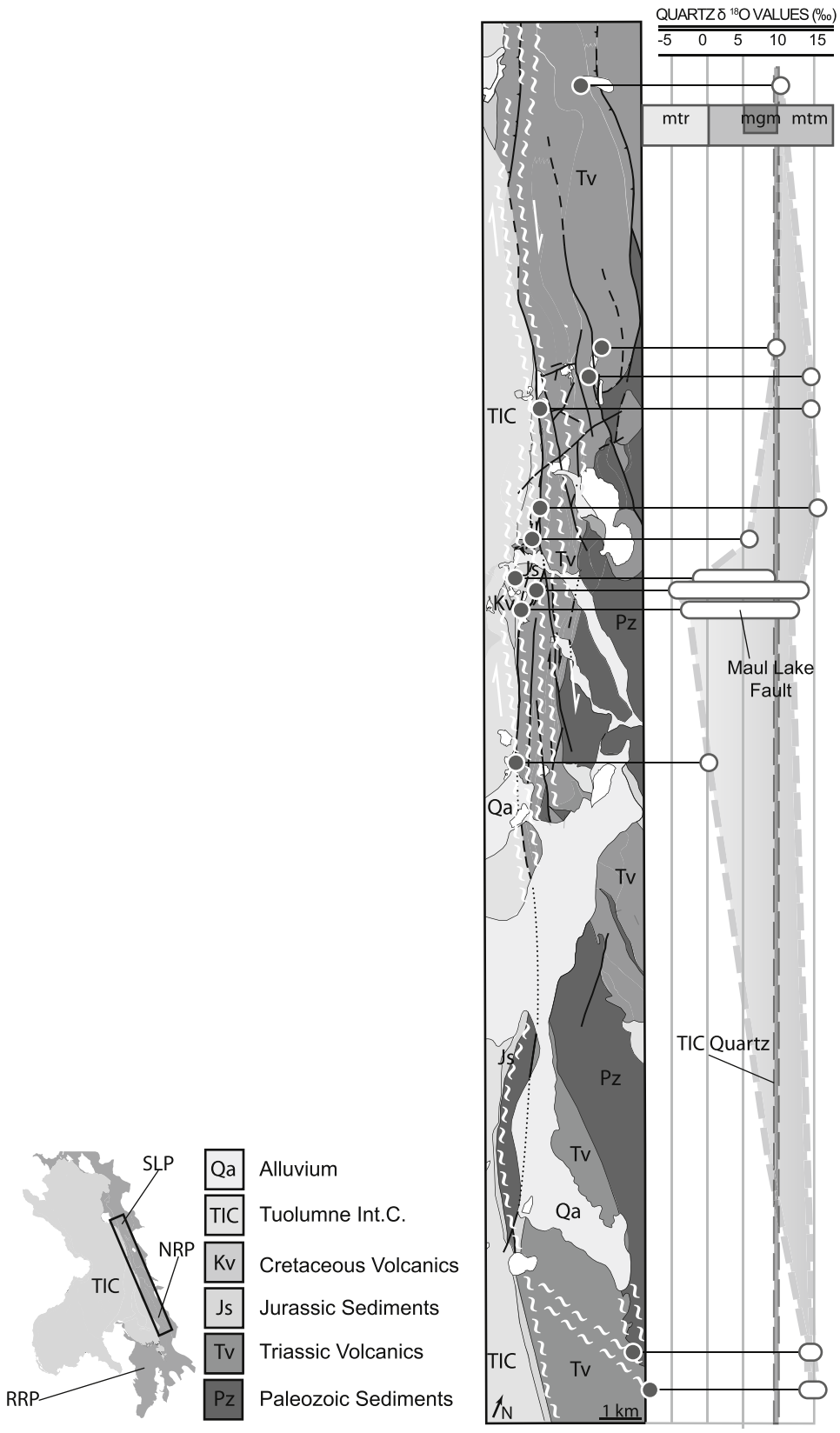

Fig. 15. Spatial distribution of $\delta^{18}O$ values (‰) in the northern Sierra Crest Shear Zone (SCSZ). The left shows a map of the SCSZ from the northern Saddlebag Lake pendant to the northern Ritter Range pendant, with the Tuolumne Intrusive Complex (TIC) bordering the pendants to the west. To the right of the map, the range of $\delta^{18}O$ values (‰) is displayed. The thin bar shows the range of quartz $\delta^{18}O$ values (‰) from the TIC (Lackey et al., 2008). The lowest oxygen isotope values are only in the Sawmill Canyon/Maul Lake area and one low value (0.8‰) was found adjacent to Granite Lakes.

Table 1
Table of $\delta^{18}O$ values (‰) for all quartz veins analyzed in the study. The left column shows all values for the Maul Lake fault, and the right column shows values for all other quartz veins, listed from top to bottom corresponding to their spatial distribution from north to south, respectively.

Maul Lake Fault Isotopes		Non-Maul Lake Fault Isotopes	
Sample	$\delta^{18}O$ (‰)	Sample	$\delta^{18}O$ (‰)
SMC-13-GI	6.6	USC-2-27	9.8
SMC-13-GI-3B	9.2	USC-7-11	9.3
SMC-13-GI-B1	7.8	SMC-13-27W	13.0
SMC-13-GI-B2	6.5	SMC-13-28-Qtz	13.0
SMC-13-HA	11.2	SMC-14-14	14.5
SMC-13-HC	9.6	SMC-14-13-Qtz	5.6
SMC-13-HD	9.7	USC-3-6	7.7
SMC-13-HG-E	8.6	USC-3-7	–0.1
SMC-13-HG-M	11.4	SMC-14-18-2	–2.5
SMC-13-HG-W	8.1	SMC-14-18-3	–1.7
SMC-14-12-BFR-W	0.7	SMC-14-18-4	–3.2
SMC-14-12-BFR-M	3.5	SMC-14-18-5	–1.5
SMC-14-12-UCC	1.2	SMC-12-07BLU	7.0
SMC-13-BP	0.8	SMC-12-31-BLU	2.3
SMC-13-EK-O	1.2	SMC-12-31-WHT	2.0
SMC-13-GB	1.7	SMC-12-32-WHT	12.3
SMC-12-45-1 Qtz	4.9	SMC-12-32-BLU	7.0
SMC-12-45-2	8.2	SMC-13-5A	9.1
SMC-12-45-4	5.1	SMC-13-5B	7.0
SMC-12-45-7	3.1	SMC-13-5C	4.1
SMC-12-45-6BLU	4.1	SMC-13-5D	12.1
SMC-12-45-11 Qtz	4.1	SMC-13-5E	11.6
SMC-12-45-3 Qtz	–0.8	SMC-13-5I	8.7
SMC-12-45-9 Qtz	4.0	SMC-13-5FQ	11.7
SMC-12-45-8 Qtz Re	3.2	SMC-14-9-1	9.5
SMC-12-45-5	4.9	SMC-14-9-2	9.4
SMC-12-45-10	5.7	SMC-14-9-3	5.6
SMC-12-45-12	3.3	SMC-14-9-4	5.3
SMC-13-EG-R	7.2	SMC-14-9-5	9.0
SMC-13-EG-W	2.5	SMC-14-9-5XTL	4.0
SMC-13-GAG	6.1	SMC-13-FQ-1-Qtz	9.1
SMC-13-BI	0.2	SMC-13-FQ-2W-Qtz	9.4
SMC-13-BN	3.4	USC-4-18	0.8
SMC-13-BQ	2.6	USC-NRA	12.7
SMC-13-EB	–1.5	USC-NRB	13.4
SMC-13-EK-W	3.4	USC-NRC	12.8
SMC-13-GAW	3.7	USC-NR-15-95	12.6
SMC-13-GI-3W	9.3	USC-NR-15-70	14.3
SMC-13-GI-W1	7.6		
SMC-13-GI-W2	0.9		

Table 2
Sample G3 $\delta^{18}O$ values (‰).

Spot	Type	$\delta^{18}O$ (‰)	Error (±)
g3@1	Qtz clast/host	12.2	0.2
g3@2	Qtz clast/host	12.3	0.2
g3@3	Qtz clast/host	11.9	0.2
g3@4	Qtz clast/host	12.5	0.1
g3@8	Qtz clast/host	12.4	0.2
g3@10	Qtz clast/host	13.0	0.2
g3@13	Qtz clast/host	13.2	0.2
g3@14	Qtz clast/host	12.7	0.2
g3@20	Qtz clast/host	12.2	0.2
g3@29	Qtz clast/host	12.9	0.1
g3@30	Qtz clast/host	12.7	0.1
g3@5	Pseudotachylyte	4.0	0.2
g3@6	Pseudotachylyte	3.5	0.2
g3@7	Pseudotachylyte	5.0	0.2
g3@9	Pseudotachylyte	3.8	0.2
g3@11	Pseudotachylyte	2.7	0.2
g3@12	Pseudotachylyte	3.1	0.3
g3@15	Pseudotachylyte	3.4	0.2
g3@16	Pseudotachylyte	3.3	0.2
g3@18	Pseudotachylyte	2.8	0.2
g3@19	Pseudotachylyte	3.2	0.1
g3@22	Pseudotachylyte	2.8	0.2
g3@23	Pseudotachylyte	2.8	0.2
g3@26	Pseudotachylyte	3.1	0.2
g3@17	Cross-cutting Qtz vein	4.1	0.1
g3@21	Cross-cutting Qtz vein	4.2	0.3
g3@24	Cross-cutting Qtz vein	4.1	0.2
g3@25	Cross-cutting Qtz vein	4.2	0.2
g3@27	Cross-cutting Qtz vein	4.0	0.2
g3@28	Cross-cutting Qtz vein	4.0	0.2

several dikes along the Triassic-Jurassic fault boundary ~1 km north of Maul Lake have also been reported (Compton et al., 2017). These reversed cross-cutting relationships indicate an overlap in the timing of magmatism (dike emplacement) and brittle fracturing and faulting. We therefore prefer this second hypothesis.

All minerals with $\delta^{18}O < 6‰$ and the lowest $\delta^{2}H$ values of quartz fluid inclusions, epidote, and tourmaline have to date only been found within the area herein interpreted as a dilational jog (Lojasiewicz, 2004; Hartman, 2017; Compton et al., 2017). More samples were analyzed from this area than in areas along the shear zone to the north and south. This sampling bias is significant, but the results are consistent with the hypothesis that the younger meteoric-hydrothermal (as opposed to older magmatic) fluids that precipitated quartz with low $\delta^{18}O$ values were focused in the dilational jog, outside of other parts of the fault zone to the north and south along strike. Fault zone permeability can be strongly controlled by active deformation disrupting sealing processes (Hickman et al., 1995; Curewitz and Karson, 1997). A simple way to explain the youngest fluids in the Sawmill Canyon segment (lowest $\delta^{18}O$ values) is that only the faults in the jog were actively deforming during ingress of meteoric-hydrothermal fluids, because mode 1 (opening) fractures acting as conduits for hydrothermal outflow followed propagating fault tips until the local stresses of newly overlapping conjugate faults interact to form a “breakdown zone” within which fluid flow becomes progressively concentrated with ongoing deformation (Curewitz and Karson, 1997). An alternative explanation is one in which fluids were focused into the low-$\delta^{18}O$ zone, interpreted as being locally transtensional while other hydrothermal fluids uncontaminated by meteoric fluids flowed out of the strike-slip faults to the north and south of the Sawmill Canyon segment, due to being locally compressed. At these depths, a fluid originating at the surface would not be a ‘meteoric fluid,’ because it would almost certainly undergo some exchange with the silicate-dominated crust during descent. In this case, the original meteoric water would have the lowest oxygen isotope ratio, which would increase by an amount determined by the water-rock ratio history and degree of mixing with other fluids (e.g. magmatic or metamorphic).

A first-order estimate of fluid volume can be made. The MLF, between Maul and Spuller Lakes, continuously crops out with a minimum width of 4 m, has an elevation change of 50 m, and a length of 300 m, yielding an estimated volume of 60,000 m^3. Using conservative values of 700 bar (assuming quartz precipitated under hydrostatic pressure during incursion from shallower depths, where $P_{Hydrostatic}$ = 700 bar, assuming $P_{Lithostatic}$ = 1900 bar (Paterson and Memeti, 2014)) and 300 °C (lower greenschist facies), orthosilicic acid is 4.4 mmol. Accordingly, 2.6 km^3 water would be required. At higher temperature, an even greater volume of water would be required.

5.2. Evolution of the ductile-to-brittle transition

Our observations indicate that the structural evolution of this system occurred in a sequence of stages that evolved as the country rock surrounding the TIC cooled following the termination of magma emplacement. The sequence is described below, and an abridged summary is shown in Fig. 5.

Early ductile (Stage 1): The first stage consisted of predominantly transpressive, dextral, and syn-magmatic to post-magmatic ductile shearing of the TIC (Tikoff et al., 2005; Cao et al., 2015) and its contemporary Mono Pass suite, which is syn-magmatically deformed by the

Rosy Finch segment of the SCSZ to the south (Tikoff and Greene, 1997). Cooling of the SCSZ to temperatures favorable for brittle faulting must have occurred after 85 Ma in the Saddlebag Lake pendant, based on magmatic and high temperature subsolidus dextral shear, dextrally sheared stoped blocks of metamorphic pendant rocks, folded and faulted dikes, and dikes that cross-cut quartz-sealed faults (Sections 3.2.1 and 3.2.3.2). During the ductile phase of deformation, dextral shear was partitioned between a main non-coaxial, dextral shear zone and smaller non-coaxial shear strands that were separated by dextral co-axial shear zones (Section 3.2.1). The total deformation, including the main non-coaxial shear zone and the partitioned smaller non-coaxial and coaxial shear zones is several km, ranging from the margin of the TIC to several km to the east. The early hot (> 700 °C), transpressive phase of deformation began prior to 85 Ma (Kerrick, 1970; Cao, 2015), and aqueous fluids flowed through veins in the host rock prior to complete termination of TIC magmatism (Fig. 10b). Heating in the country rock resulting from 10 myr of magma emplacement in the TIC activated plastic deformation mechanisms such as dislocation creep in quartz and likely dislocation glide in phyllosilicates to accommodate transpressive strain within a 1–2 km wide NNW-striking deformation zone in the Saddlebag Lake pendant (Compton et al., 2017).

Deformation of 88–85 Ma (Kistler and Fleck, 1994; Coleman et al., 2004; Memeti et al., 2010) Cathedral Peak phase dikes provide helpful clues about the timing of different deformation types in the Saddlebag Lake pendant. A calculated high-precision chemical abrasion isotope dilution thermal ionization mass spectrometry (CA-ID-TIMS) zircon age of 88.5 Ma was measured in a characteristic dike near Steelhead Lake (Paterson and Memeti, 2014), indicating that these dikes are likely related to the Cathedral Peak unit of the TIC. In the same area, a Cathedral Peak dike with plastic shear deformation has reset $^{40}Ar/^{39}Ar$ biotite cooling ages of 83.7 ± 0.3 Ma and 84.4 ± 0.2 Ma in fine- and coarse-grained biotites, respectively (Paterson and Memeti, 2014). Cathedral Peak phase (88-86 Ma) dikes west of the Steelhead Lake fault are folded and have subsolidus, subvertical metamorphic stretching lineations, which is consistent with the lineations in the host rock.

The deformation that occurred as a result in the Saddlebag Lake pendant was largely partitioned into coaxial and non-coaxial ductile shear in the units of varying competency. This is evidenced by isoclinal and symmetrical folds of late TIC dikes and hydrothermal veins, coaxial deformation of Late Cretaceous rocks, the same metamorphic minerals defining both coaxial and non-coaxial fabrics, and the overlapping $^{40}Ar/^{39}Ar$ hornblende and biotite ages in the Gem Lake segment of the SCSZ (Sharp et al., 2000). Metamorphic fluids were present outside of the shear zone (Lojasiewicz et al., 2016), and magmatic fluids precipitated veins that were subsequently recrystallized, sheared, and folded (Compton et al., 2017).

Late ductile/early transitional (Stage 1.5): The late ductile/early transitional stage was characterized by ductile shearing with syn-kinematic foliation-parallel and discordant veins and dikes following TIC cooling to below the solidus. Fracturing was heavily influenced by mechanical anisotropy of rock due to aligned phyllosilicates in spaced and continuous cleavages in the different lithologies (Compton et al., 2017). Alteration of surrounding host rock occurred in the form of leaching, especially around tourmaline veins (Fig. 6h). Vertical or subvertical brittle fault conduits at shallower levels presumably descended by fault propagation. Fluid flow in fractures at the Sawmill Canyon depth is inferred to have been localized in many small channels formed by fractures, and alter.

Transitional (Stage 2): Outcrop- and larger-scale faults evolved from thin shear zones due to mechanical heterogeneity arising from competency contrasts, layering, or contacts between different lithologies. Some fractures cut lithologies and juxtapose blocks of the same unit (e.g. the MLF between Maul and Spuller Lake, Fig. 4). Stratigraphic contacts are also interpreted as reactivated unconformities (Cao, 2015). Fault zone geometric heterogeneities (such as folds and stratigraphic discontinuities, Fig. 2) in the Sawmill Canyon segment began inducing dilation of faults, causing some to connect to shallower faults containing meteoric-hydrothermal fluids.

These brittle faults and their shallower counterparts are inferred to have connected the shallower meteoric-hydrothermal fluids, initiating their descent into the Sawmill Canyon-level of the crust. Where the strike-slip faults overlapped across strike, a dilational jog zone was initiated. This zone became a local sink for meteoric-hydrothermal fluid. Fluids began transitioning from a dominantly magmatic fluid source to one with a meteoric-hydrothermal component, but only in the jog (Fig. 15; Lojasiewicz et al., 2016; Compton et al., 2017; this work). Meteoric-hydrothermal fluids were already present before crystalplastic deformation was terminated due to cooling (Compton et al., 2017).

Recrystallization may have influenced the oxygen isotope ratios, but it occurred at temperatures between 400 and 500 °C, meaning the greatest oxygen isotope fractionation factor between quartz and water would be 4.2‰ (Sharp et al., 2016). The lowest calculated fluid $\delta^{18}O$ value (−2.0‰) would, in this case, only be elevated to 2.2‰, and it could only be elevated to this value by complete equilibration. Therefore, even given this re-equilibration scenario took place, we still consider precipitation from meteoric-hydrothermal fluids to be the best explanation for these veins.

Late transitional/early brittle (Stage 2.5): In the late transitional/early brittle stage, offsets across the main strike-slip fault strands caused the secondary N- to NE-oriented faults to develop in the Sawmill Canyon segment (Fig. 2). Meteoric-hydrothermal fluid ingress appears to have been focused to the jog that geographically spans from the Sawmill Canyon to Granite Lakes segments, based on exceptionally low quartz $\delta^{18}O$ values (Fig. 15), and calculated fluid $\delta^{18}O$ values < 0‰ (Compton et al., 2017).

Earthquakes occurred to produce pseudotachylyte in the presence of a meteoric-hydrothermal fluid mixture before the fluids were entirely dominated by the meteoric-hydrothermal end member. Quartz clasts ($\delta^{18}O$ = 12.6‰) within the pseudotachylyte ($\delta^{18}O$ = 3.3‰) demonstrate no isotopic evidence of interaction with meteoric-hydrothermal fluids, but the younger quartz veins ($\delta^{18}O$ = 4.2‰) that cross-cut the other two phases, have $\delta^{18}O$ values too low to be in equilibrium with anything other than meteoric-hydrothermal fluids at geologically reasonable temperatures. This is also true for the pseudotachylyte phase, which also has $\delta^{2}H$ < −137‰, a value only known to exist in meteoric and meteoric-hydrothermal fluids (Craig, 1961). This may reflect either the presence of a meteoric-hydrothermal fluid during the formation of the pseudotachylyte, or formation of pseudotachylyte from a meteoric-hydrothermally altered protolith. The fact that the younger cross-cutting quartz veins indicate meteoric-hydrothermal fluids, but have far from the lowest $\delta^{18}O$ values for quartz veins in the fault zone ($\delta^{18}O$ = −1.5‰ in the same fault, $\delta^{18}O$ = −3.2‰ in the area) is evidence that earthquakes occurred prior to the final stages of fluid flow and faulting.

Brittle (Stage 3): Most of the deformation was accommodated by slip and dilation of the main fault strands, especially the quartz-sealed (11.5 m wide at its widest) MLF. Slip on the main strand of the MLF caused fractures to form in a damage zone, into which fluids continued to infiltrate. This process probably initiated before the final brittle Stage 3 of deformation, based on the range of quartz $\delta^{18}O$ values within this composite vein. Cross-cutting relationships indicate that the composite veins young inward (Fig. 12 b, c), and correlate with decrease in $\delta^{18}O$ over time. Meteoric-hydrothermal fluids flowed through the oblique intra-jog faults, local outcrop-scale jogs (Fig. 9), and the main fault strand (MLF, Fig. 12) where it overlaps with the Steelhead Lake fault along strike (Figs. 2 and 4).

The oblique sinistral brittle faults consistently crosscut NNE-striking faults where the two intersect (Fig. 8d). This suggests the minor antithetic slip component was operative in the latest brittle stage. These youngest oblique, sinistral, brittle faults are compatible with faults in the Rosy Finch segment in the Lake Edison area where a northeast-striking dextral kink zone defined by kinking of oblique sinistral faults

overprints the ductile shear zone. Fault vein muscovite (Segall et al., 1990) and sericite (Pachell et al., 2003) samples have K-Ar and $^{40}Ar/^{39}Ar$ ages of 79 Ma, representing cooling below the closure temperature ~350 °C. The trend of the kink zone is 333, similar to the average strike of the ductile shear zone (346) and brittle faults (348) in the western Saddlebag Lake pendant. This orientation and the dextral offset (accommodated by oblique sinistral faults) are consistent with the brittle faulting in the Saddlebag Lake pendant. This therefore implies that the oblique sinistral faults in the Sawmill Canyon segment are compatible with dextral transpression.

5.3. Structural controls on fluid flow and seismicity

The widest quartz veins, the greatest-wavelength and most well-developed folds, and the only $\delta^{18}O$ values demonstrating interaction with meteoric-hydrothermal fluids are confined to the jog. We suggest that these features are related and were caused by shear zone and fault zone heterogeneities leading to local dilation of faults at this brittle-ductile transition. Two-dimensional photoelastic experiments have been used to model the permeability structure of a developing jog, and demonstrate that fluid flow is inhibited before the tips of the connecting strike-slip faults overlap, but once overlap is achieved, the intra-jog region's permeability dramatically increases (Connolly and Cosgrove, 1999). In addition, the flanking strike-slip faults connected by the intra-jog oblique faults could become significant fluid conduits in terms of the volume flux of fluids circulating through them relative to other faults in the system, based on the large quartz veins. The northern tip of the MLF, which is the widest quartz vein we have discovered (locally > 11 m wide), demonstrates evidence for enhanced fluid flow in the overlapping rupture terminus of a flanking strike-slip fault bounding a jog. The MLF clearly formed over a series of events. Single events in jogs, such as dilation during co-seismic ruptures, can be accompanied by fluid pressure oscillations that assist in fluid mixing (Boiron et al., 2003) and drawing in of fluids toward the hydraulic anomaly (Weatherly and Henley, 2013), which may promote descent of shallower meteoric-hydrothermal fluids to greater depths in a fault zone.

Strike-slip deformation at the depth of the brittle-ductile transition is widely interpreted to be near the peak strength of the crust, above which brittle deformation is a function of confining pressure, and below which plastic deformation is controlled by temperature (Sibson, 1982). A more realistic model of this transition involves a combination of both brittle and ductile deformation mechanisms overlapping, which can closely coexist and even overlap in time and space (e.g. Druguet et al., 2009). Crustal strength and seismic potential are generally near the bases of brittle and seismic layers because the amount of elastic energy that can be released increases with depth (Sibson, 1982). Additionally, fluids play a profound role in seismic fault zones because they weaken faults by reducing the effective stress. Our results therefore support the hypothesis that geometric heterogeneities caused by fault-step overs can behave as conduits that may connect large volumes of surface fluids to the ductile crust, which may in turn have the effect of lowering the brittle-ductile transition, and thus increasing the seismic potential of the fault zone.

Debate about the conditions of pseudotachylyte generation is ongoing. A key factor in generating pseudotachylytes may be the absence of intergranular fluids, because they have the capacity to dramatically reduce effective normal stresses and thus heat dissipation during frictional sliding (Sibson, 1975). This stands in contrast with experimental results and theoretical considerations (e.g. Philpotts, 1964; Goodwin, 1999; O'Hara and Sharp, 2001; Bjørnerud, 2010; Violay et al., 2014). Instead, pseudotachylyte formation may be common but obscured by subsequent deformation (Kirkpatrick and Rowe, 2013), or rarely recognized (Kirkpatrick et al., 2009). The presence of meteoric water during the generation of pseudotachylyte sample G3 (Fig. 14) cannot be demonstrated using only $\delta^{18}O$ values, because the bulk chemical composition of pseudotachylyte matrix, un-melted lithic clasts, and surrounding protolith must be known (Moecher and Sharp, 2004).

The $\delta^{18}O$ values of the three different phases in pseudotachylyte sample G3 from the Saddlebag Lake pendant (protolith $\delta^{18}O$ = 12.6‰, pseudotachylyte matrix $\delta^{18}O$ = 3.3‰, younger quartz vein $\delta^{18}O$ = 4.1‰), combined with the $\delta^{2}H$ values for the pseudotachylyte matrix ($\delta^{2}H$ = −137‰), strongly indicate that meteoric-hydrothermal water interacted with this rock prior to (e.g. Di Toro and Pennacchioni, 2005) or during the generation of the pseudotachylyte (e.g. Goodwin, 1999). In either case, the pseudotachylyte and cross-cutting quartz vein stable isotope data suggest that meteoric-hydrothermal fluids had infiltrated the fault zone both before and after pseudotachylyte formation. The consistent $\delta^{18}O$ value of 3.3‰ for the younger quartz veins that cross cut the pseudotachylyte (4.1‰) is significantly higher than the lowest $\delta^{18}O$ values for quartz veins in this fault system (−3.5‰). This indicates that the pseudotachylyte formed before the mixing process completely transitioned to meteoric-hydrothermal fluids, meaning that the fault zone would have been seismogenic within the time window during which the fluids flowing in this system evolved and incorporated a meteoric-hydrothermal source.

Fluids profoundly affect deformation mechanisms and seismicity, as long as they are capable of interaction with the deforming rocks. At the level of the brittle-ductile transition and in a tectonically compressed fault zone, access to a fluid with an abundant reservoir such as meteoric-hydrothermal water has been demonstrated by stable isotope studies (Lobato et al., 1983; Menzies et al., 2014). The spatial correlation with shear zone and fault zone heterogeneity, the widest quartz veins, the concentration of low quartz $\delta^{18}O$ values, the presence of low $\delta^{18}O$ value-quartz that has been recrystallized in the shear zone, and the overlapping of the flanking main fault strands to define the jog, suggest that local descent of fluids derived from the surface was structurally controlled and permitted by local transtension in a segment of the SCSZ wherein shear zone heterogeneity may have initiated the development of the jog.

6. Conclusions

Mapping, field observations, and structural analysis indicate a rheological transition from ductile to brittle deformation associated with cooling of the western Saddlebag Lake pendant. Cooling from the ~700 °C solidus of the 88-85 Ma Cathedral Peak phases of the TIC and associated heating, metamorphism, and limited partial melting (Albertz, 2006) of the Saddlebag Lake pendant, cooled to sub-greenschist facies conditions by ~80 Ma (Cao et al., 2015), which is consistent with other well-studied segments of the SCSZ. The brittle-ductile fault zone is characterized by an immature strike-slip duplex and a dilational jog. The $\delta^{18}O$ values of quartz veins indicate that meteoric-hydrothermal fluids were focused to the jog, and $\delta^{18}O$ and $\delta^{2}H$ values of pseudotachylyte indicate that earthquakes occurred during the flow of meteoric-hydrothermal fluids. These observations are consistent with a structural model (Fig. 5) that permits the incursion of meteoric-hydrothermal fluids to the base of the seismogenic crust in a strike-slip fault zone.

Acknowledgements

We gratefully acknowledge support for this work by NSF grant 0949044, USGS EDMAP grants G13AC00120 and G15AC00134, internal research funding from California State University, Long Beach, and a 2015 GSA graduate student research grant. We thank Yosemite Valley National Park for sampling permissions. Additionally, we thank Snir Attia, Katie Ardill, Iwo Lojasiewicz, Katharine Compton, Gus Womeldorph, and Colin Campbell for field assistance and insightful feedback, and Jade-Star Lackey, Kyle McCarty, and Jonathan Harris for assistance and use of facilities at the Pomona College Oxtoby environmental isotope laboratory. Finally, we warmly thank Ian Alsop,

Catriona Menzies, and an anonymous reviewer for their insightful and constructive feedback.

References

Ague, J.J., Brimhall, G.H., 1988. Magmatic arc asymmetry and distribution of anomalous plutonic belts in the batholiths of California: effects of assimilation, crustal thickness, and depth of crystallization. Geol. Soc. Am. Bull. 100, 912–927.

Albertz, M., 2006. Relationships between melt-induced rheological transitions and finite strain: observations from host rock pendants of the Tuolumne Intrusive Suite, Sierra Nevada, California. J. Struct. Geol. 28, 1422–1444.

Anderson, J.L., Foley, B., Ball, E.N., Paterson, S.R., Memeti, V., Pignotta, G.S., 2007. Upper Crustal Overturn during Magmatic Surges - a Potential Sierra-wide Process 39. pp. 6 GSA Abstracts with Programs.

Attia, S., Paterson, S.R., Cao, W., Chapman, A.D., Saleeby, J., Dunne, G.C., Steven, C.H., Memeti, V., 2018;al., In Press. Late Paleozoic Tectonic Assembly of the Sierra Nevada Prebatholithic Framework and Western Laurentian Provenance Links Based on Synthesized Detrital Zircon Geochronology. GSA Special Paper. In Press.

Behr, W.M., Platt, J.P., 2014. Brittle faults are weak, yet the ductile middle crust is strong: implications for lithospheric mechanics. Geophys. Res. Lett. 41 (22), 8067–8075.

Bentley, C., 2004. Rock Fabric Analysis of the Sierra Crest Shear Zone System, California: Implications for Crustal-scale Transpressional Shear Zones. Master's thesis. University of Maryland, College Park.

Bjørnerud, M., 2010. Rethinking conditions necessary for pseudotachylyte formation: observations from the Otago schists, South Island, New Zealand. Tectonophysics 490 (1), 69–80.

Boiron, M.C., Cathelineau, M., Banks, D.A., Fourcade, S., Vallance, J., 2003. Mixing of metamorphic and surficial fluids during the uplift of the Hercynian upper crust: consequences for gold deposition. Chem. Geol. 194, 119–141.

Brathwaite, R.L., McKay, D.F., Henderson, S., 1986. The martha Hill gold-silver deposit, Waihi. In: Brathwaite, R.L., Browne, P.R.L., Roberts, P.J. (Eds.), Proceedings of Symposium 5: Volcanism, Hydrothermal Systems, and Related Mineralization. University of Auckland, International Volcanological Congress, pp. 19–23.

Brook, C.A., 1977. Stratigraphy and structure of the Saddlebag Lake roof pendant, Sierra Nevada, California. Geol. Soc. Am. Bull. 88, 321–334.

Cao, W., 2015. Links, Tempos, and Mass Balances of Cyclic Deformation and Magmatism in Arcs: a Case Study on the Mesozoic Sierra Nevada Arc Integrating Geologic Mapping, Geochronology, Geobarometry, Strain Analyses and Numerical Simulations. PhD thesis. University of Southern California.

Cao, W., Paterson, S.R., Memeti, V., Mundil, R., Anderson, L., Schmidt, K., 2015. Tracking paleodeformation fields in the Mesozoic central Sierra Nevada arc: implications for intra-arc cyclic deformation and arc tempos. Lithosphere 7, 296–320.

Cao, W., Paterson, S., Saleeby, J., Zalunardo, S., 2016. Bulk arc strain, crustal thickening, magma emplacement, and mass balances in the Mesozoic Sierra Nevada arc. J. Struct. Geol. 84, 14–30.

Cardozo, N., Allmendinger, R.W., 2013. Spherical projections with OSXStereonet. Comput. Geosci. 51, 193–205.

Cecil, M.R., Ducea, M.N., Reiners, P.W., Chase, C.G., 2006. Cenozoic exhumation of the northern Sierra Nevada, California, from (U-Th)/He thermochronology. Geol. Soc. Am. Bull. 118, 1481–1488.

Coleman, D.S., Glazner, A.F., 1997. The Sierra Crest magmatic event: rapid formation of juvenile crust during the Late Cretaceous in California. Int. Geol. Rev. 39, 768–787.

Coleman, D.S., Gray, W., Glazner, A.F., 2004. Rethinking the emplacement and evolution of zoned plutons: geochronologic evidence for incremental assembly of the Tuolumne intrusive suite, California. Geology 32 (5), 433–436. http://dx.doi.org/10.1130/G20220.1.

Compton, K.E., Kirkpatrick, J.D., Holk, G.J., 2017. Cyclical shear fracture and viscous flow during transitional ductile-brittle deformation in the Saddlebag Lake shear zone, California. Tectonophysics 708, 1–14.

Connolly, P., Cosgrove, J., 1999. Prediction of fracture-induced permeability and fluid flow in the crust using experimental stress data. AAPG Bulletin 83 (5), 757–777.

Craig, H., 1961. Isotopic variations in meteoric waters. Science 133 (3465), 1702–1703.

Curewitz, D., Karson, J.A., 1997. Structural settings of hydrothermal outflow: fracture permeability maintained by fault propagation and interaction. J. Volcanol. Geoth. Res. 79, 149–168.

Di Toro, G., Pennacchioni, G., 2005. Fault plane processes and mesoscopic structure of a strong-type seismogenic fault in tonalites (Adamello batholith, Southern Alps). Tectonophysics 402 (1), 55–80.

Dieterich, J.H., 1974. Earthquake mechanisms and modelling. In: In: Donath, F.A. (Ed.), Annual Review of Earth and Planetary Science, vol. 2. Annual Reviews Inc., Palo Alto, California, pp. 275–301.

Druguet, E., Alsop, G.I., Carreras, J., 2009. Coeval brittle and ductile structures associated with extreme deformation partitioning in a multilayer sequence. J. Struct. Geol. 31 (5), 498–511.

Doblas, M., 1998. Slickenside kinematic indicators. Tectonophysics 295 (1), 187–197.

Ducea, M., 2001. The California arc: thick granitic batholiths, eclogitic residues, lithospheric-scale thrusting, and magmatic flare-ups. GSA Today 11 (11), 4–10.

Fusseis, F., Handy, M.R., 2008. Micromechanisms of shear zone propagation at the brittle-viscous transition. J. Struct. Geol. 30, 1242–1253.

Gébelin, A., Mulch, A., Teyssier, C., Heizler, M., Vennemann, T., Seaton, N.C.A., 2011. Oligo-Miocene extensional tectonics and fluid flow across the Northern Snake Range detachment system, Nevada. Tectonics 30, TC5010. http://dx.doi.org/10.1029/2010TC002797.

Goodwin, L.B., 1999. Controls on pseudotachylyte formation during tectonic exhumation in the South Mountains metamorphic core complex, Arizona. In: In: Ring, U., Brandon, M.T., Lister, G.S., Willett, S.D. (Eds.), Exhumation Processes: normal Faulting, Ductile Flow and Erosion, vol. 154. Geological Society, London, Special Publications, pp. 325–342.

Gratier, J.P., Richard, J., Renard, F., Mittempergher, S., Doan, M.L., Di Toro, G., Hadizadeh, J., Boullier, A.M., 2011. Aseismic sliding of active faults by pressure solution creep: evidence from the san Andreas fault observatory at depth. Geology 39 (12), 1131–1134.

Gray, W.M., 2003. Chemical and thermal Evolution of the Late Cretaceous Tuolumne Intrusive Suite, Yosemite National Park. Ph.D. thesis. Chapel Hill, University of North Carolina, California.

Greene, D.C., Schweickert, R.A., 1995. The Gem Lake shear zone - cretaceous dextral transpression in the northern ritter range pendant, eastern Sierra-Nevada California. Tectonics 14 (4), 945–961.

Harrison, T.M., 1981. Diffusion of 40Ar in Hornblende: Contributions to Mineralogy and Petrology. vol. 78. pp. 324–331.

Harrison, T.M., Duncan, I., McDougall, I., 1985. Diffusion of 40Ar in biotite: temperature, pressure, and compositional effects. Geochem. Cosmochim. Acta 49, 2461–2468.

Hartman, S.M., 2017. Fluid and Structural Evolution of Late Cretaceous Cordilleran Ductile-brittle Shear Zones in Hot and Cooling Orogens: Examples from the Sierra Nevada, CA and Cascades Crystalline Core. Ph.D. thesis. University of Southern California, WA.

Hickman, S., Sibson, R., Bruhn, R., 1995. Introduction to Special Section: Mechanical Involvement of Fluids in Faulting. USGS Staff – Published Research. 410. pp. 12 831-12,840.

Holk, G.J., Taylor, H.P., 2007. $^{18}O/^{16}O$ Evidence for contrasting hydrothermal regimes involving magmatic and meteoric-hydrothermal waters at the Valhalla Metamorphic Core Complex, British Columbia. Econ. Geol. 102, 1063–1078.

Holk, G.J., Grove, M., Jacobson, C.E., Haxel, G.B., 2017. A two-stage fluid history for the Orocopia Schist and associated rocks related to flat subduction and exhumation, southeastern California. Int. Geol. Rev. 59, 639–663.

Horsman, E., Tikoff, B., Czeck, D., 2008. Rheological implications of heterogeneous deformation at multiple scales in the Late Cretaceous Sierra Nevada, California. Geol. Soc. Am. Bull. 120, 238–255.

Huber, N.K., Bateman, P.C., Wahrhaftig, C., 1989. Geologic Map of Yosemite National Park and Vicinity, California. U.S. Geological Survey Miscellaneous Investigations Series Map I-1874, 1:125,000 scale.

Jiang, D., Bentley, C., 2012. A micromechanical approach for simulating multiscale fabrics in large-scale high-strain zones: theory and application. Journal of Geophysical Research, Res. 117, B12201.

Kerrick, D.M., 1970. Contact metamorphism in some areas of the Sierra Nevada, California. Geol. Soc. Am. Bull. 81 (10), 2913–2938.

Kirkpatrick, J.D., Rowe, C.D., 2013. Disappearing ink: How pseudotachylytes are lost from the rock record. J. Struct. Geol. 52, 183–198.

Kirkpatrick, J.D., Shipton, Z.K., Persano, C., 2009. Pseudotachylytes: rarely generated, rarely preserved, or rarely reported? Bull. Seismol. Soc. Am. 99, 382–388. http://dx.doi.org/10.1785/0120080114.21.

Kistler, R.W., Fleck, R.J., 1994. Field guide for a transect of the central Sierra Nevada, California: geochronology and isotope geology. U.S. Geological Survey Open-File Report 94 (267), 54.

Lackey, J.S., Valley, J.W., Chen, J.H., Stockli, D.F., 2008. Evolving magma systems, crustal recycling, and alteration in the central Sierra Nevada batholith: the oxygen isotope record. J. Petrol. 49, 1397–1426.

Lobato, L.M., Forman, J.M.A., Fyfe, W.S., Kerrich, R., Barnett, R.L., 1983. Uranium enrichment in Archaean crustal basement associated with overthrusting. Nature 303, 235–237.

Lojasiewicz, I., 2004. A Stable Isotope Study of Fluid-rock Interactions in the Saddlebag Lake Roof Pendant, Sierra Nevada, California. Master's thesis. California State University Long Beach.

Lojasiewicz, I., Hartman, S.M., Holk, G.J., Paterson, S.R., 2016. A Stable Isotope Study of Fluid-rock Interactions in the Saddlebag Lake Roof Pendant, Sierra Nevada. AGU Fall Meeting Abstract, California T31F-2909.

Mancktelow, N.S., Pennacchioni, G., 2005. The control of precursor brittle fracture and fluid-rock interaction on the development of single and paired ductile shear zones. J. Struct. Geol. 27 (4), 645–661.

McCaig, A.M., 1988. Deep fluid circulation in fault zones. Geology 16, 867–870.

McNulty, B.A., 1995. Shear zone development during magmatic arc construction: the Bench Canyon shear zone, central Sierra Nevada, California. Geol. Soc. Am. Bull. 107 (9), 1094–1107.

Memeti, V., Economos, R.C., Erdmann, S., Paterson, S.R., Miller, R.B., 2005. Regional and emplacement related tectonism during intrusion of the Tuolumne batholith: results from the Benson Lake and may lake pendants, Sierra Nevada, California. Geol. Soc. Am. Abstr. Progr. 37 (4), 70.

Memeti, V., Paterson, S.R., Matzel, J., Mundil, R., Okaya, D., 2010. Magmatic lobes as "snapshots" of magma chamber growth and evolution in large composite batholiths: an example from the Tuolumne Intrusion, Sierra Nevada, CA. Geol. Soc. Am. Bull. 122 (11–12), 1912–1931.

Menzies, C.D., Teagle, D.A.H., Craw, D., Cox, S.C., Boyce, A.J., Barrie, C.D., Roberts, S., 2014. Incursion of meteoric waters into the ductile regime in an active orogen. Earth Planet Sci. Lett. 399, 1–13.

Miller, J.S., Matzel, J.E., Miller, C.F., Burgess, S.D., Miller, R.B., 2007. Zircon growth and recycling during the assembly of large, composite arc plutons. J. Volcanol. Geoth. Res. 167 (1), 282–299.

Moecher, D.P., Sharp, Z.D., 2004. Stable isotope and chemical systematics of pseudotachylyte and wall rock, homestake shear zone, Colorado, USA: meteoric fluid or rock-buffered conditions during coseismic fusion? J. Geophys. Res. 109, 1–11.

Morrison, J., 1994. Meteoric water-rock interaction in the lower plate of the Whipple Mountain metamorphic core complex, California. J. Metamorphic Petrology 12 (6), 827–840.
Matzel, J., Mundil, R., Paterson, S., Renne, P., Nomade, S., 2005. Evaluating pluton growth models using high precision geochronology: Tuolumne Intrusive Suite, Sierra Nevada, CA. Geol. Soc. Am. 37, 131 Abstracts with Programs.
Matzel, J., Miller, J.S., Mundil, R., Paterson, S.R., 2006. Zircon saturation and the growth of the Cathedral Peak pluton. Geochim. Cosmochim. Acta 70 (18), A403.
Nadin, E.S., Saleeby, J., Wong, M., 2016. Thermal evolution of the Sierra Nevada batholith, California, and implications for strain localization. Geosphere 12 (2), 377–399.
Norton, D.L., 1984. Theory of hydrothermal systems. Annu. Rev. Earth Planet Sci. 12, 155–177.
O' Hara, K.D., Sharp, Z.D., 2001. Chemical and oxygen isotope composition of natural and artificial pseudotachylyte: role of water during frictional fusion. Earth Planet Sci. Lett. 184, 393–406.
Pachell, M.A., Evans, J.P., Taylor, W.L., 2003. Kilometer-scale kinking of crystalline rocks in a transpressive convergent setting, central Sierra Nevada, California. Geol. Soc. Am. Bull. 115 (7), 817–831. http://dx.doi.org/10.1130/0016-7606(2003)115<0817:KKOCRI>2.0.CO;2.
Paterson, S.R., Memeti, V., 2014. Day 5: mesozoic volcanic rocks of the central Sierra Nevada arc. In: Formation of the Sierra Nevada Batholith: Magmatic and Tectonic Processes and Their Tempos, vol. 34. Geological Society of America Field Guide, pp. 75–82.
Paterson, S.R., Memeti, V., Anderson, L., Cao, W., Lackey, J.S., Putirka, K.D., Mundil, R., 2014. Day 6: overview of arc processes and tempos. In: Formation of the Sierra Nevada Batholith: Magmatic and Tectonic Processes and Their Tempos, vol. 34. Society of America Field Guide, pp. 87–116. http://dx.doi.org/10.1130/2014.0034(06.
Peng, Z., Gomberg, J., 2010. An integrated perspective of the continuum between earthquakes and slow-slip phenomena. Nat. Geosci. 3, 599–607.
Philpotts, A.R., 1964. Origin of pseudotachylytes. Am. J. Sci. 262 (8), 1008–1035.
Rose, R.L., 1957. Andalusite and corundum-bearing pegmatites in Yosemite National Park, California. Am. Mineral. 42, 635–647.
Schweickert, R.A., Lahren, M.M., 1993. Tectonics of the east-central Sierra Nevada - Saddlebag Lake and northern ritter range pendants. In: Lahren, M.M., Trexler Jr.J.H., Spinosa, C. (Eds.), Crustal Evolution of the Great Basin and Sierra Nevada: Cordilleran/Rocky Mountains Section. Geological Society of America Guidebook, Department of Geological Sciences, University of Nevada, Reno, pp. 313–351.
Schweickert, R.A., Lahren, M.M., 2006. Geologic evolution of Saddlebag Lake pendant, eastern Sierra Nevada, California: tectonic implications. In: In: Girty, G.H., Cooper, J.D. (Eds.), Using Stratigraphy, Sedimentology, and Geochemistry to Unravel the Geologic History of the Southwestern Cordillera. Pacific Section, vol. 101. SEPM (Society for Sedimentary Geology) Publication, pp. 27–56.
Segall, P., McKee, E.H., Martel, S.J., Turrin, B.D., 1990. Late Cretaceous age of fractures in the Sierra Nevada batholith, California. Geology 18 (12), 1248–1251.
Sharp, W.D., Tobisch, O.T., Renne, P.R., 2000. Development of Cretaceous transpressional cleavage synchronous with batholith emplacement, central Sierra Nevada, California. Geol. Soc. Am. Bull. 112 (7), 1059–1066.
Sharp, Z.D., 1990. A laser-based microanalytical method for the in-situ determination of oxygen isotope ratios of silicates and oxides. Geochem. Cosmochim. Acta 54 (5), 1353–1357.
Sharp, Z.D., Gibbons, J.A., Maltsev, O., Atudorei, V., Pack, A., Sengupta, S., Shock, E.L., Knauth, L.P., 2016. A calibration of the triple oxygen isotope fractionation in the SiO2-H2O system and applications to natural samples. Geochem. Cosmochim. Acta 186, 105–119.
Sibson, R.H., 1975. Generation of pseudotachylyte by ancient seismic faulting. Geophys. J. Roy. Astron. Soc. 43, 775–794.
Sibson, R.H., 1981. Controls on low-stress hydro-fracture dilatancy in thrust, wrench, and normal-fault terrains. Nature 289, 665–667.
Sibson, R.H., 1982. Fault zone models, heat flow, and the depth distribution of earthquakes in the continental crust of the United States. Bull. Seismol. Soc. Am. 72 (1), 151–163.
Sibson, R.H., 1987. Earthquake rupturing as a mineralizing agent in hydrothermal systems. Geology 15, 701–704.
Sibson, R.H., Robert, F., Poulsen, K.H., 1988. High-angle reverse faults, fluid-pressure cycling, and mesothermal gold-quartz deposits. Geology 16, 551–555.
Soden, A.M., Shipton, Z.K., Lunn, R.J., Pytharouli, S.I., Kirkpatrick, J.D., Do Nascimento, A.F., Bezerra, F.H.R., 2014. Brittle structures focused on subtle crustal heterogeneities: implications for flow in fractured rocks. J. Geol. Soc. 171 (4), 509–524.
Spruzeniece, L., Piazolo, S., 2015. Strain localization in brittle-ductile shear zones: fluid abundant vs. fluid-limited conditions (an example from Wyangala area, Australia). Solid Earth 6, 881–901.
Tikoff, B., 1994. Transpression Strain Theory and Application to the Emplacement and Deformation of Granite, Sierra Nevada. Ph.D. thesis. University of Minnesota, California Minneapolis.
Tikoff, B., Davis, M.R., Teyssier, C., de St Blanquat, M., Habert, G., Morgan, S., 2005. Fabric studies within the cascade lake shear zone, Sierra Nevada, California. Tectonophysics 400, 209–226.
Tikoff, B., de Saint Blanquat, M., 1997. Transpressional shearing and strike-slip partitioning in the Late Cretaceous Sierra Nevada magmatic arc, California. Tectonics 16 (3), 442–459.
Tikoff, B., Greene, D., 1997. Stretching lineations in transpressional shear zones: an example from the Sierra Nevada Batholith, California. J. Struct. Geol. 19, 29–40.
Tikoff, B., Teyssier, C., 1992. Crustal-scale en echelon "P-shear" tensional bridges: a possible solution to the batholithic room problem. Geology 20, 927–930.
Tobisch, O.T., Saleeby, J.B., Renne, P.R., McNulty, B., Tong, W., 1995. Variations in deformation fields during development of a large volume magmatic arc, central Sierra Nevada, California. Geol. Soc. Am. Bull. 107, 148–166.
Tucker, W.B., Sampson, R.J., 1940. Mineral Resources of Mono County: California Journal of Mines and Geology (Report 36): 36, 2, 139. California Division of Mines.
Violay, M., Nielsen, S., Gibert, B., Spagnuolo, E., Cavallo, A., Azais, P., Vinciguerra, S., Di Toro, G., 2014. Effect of water on the frictional behavior of cohesive rocks during earthquakes. Geology 42 (1), 27–30. http://dx.doi.org/10.1130/G34916.1.
Weatherly, D.K., Henley, R.W., 2013. Flash vaporization during earthquakes evidenced by gold deposits. Nat. Geosci. 6, 294–298. http://dx.doi.org/10.1038/ngeo1759.
Webber, C.E., Candela, P.A., Piccoli, P.M., Simon, A.C., 2001. Generation of granitic dikes: can microstructure, mineralogy, and geochemistry be used as guides to determine the mechanisms of diking? Geol. Soc. Am. Abstr. Progr. 33 (6), 138.
Wech, A.G., Boese, C.M., Stern, T.A., Townend, J., 2012. Tectonic tremor and deep slow slip on the Alpine fault. Geophys. Res. Lett. 39 (10), 1–6.
Whitesides, A.S., Cao, W., Paterson, S.R., 2010. Pseudotachylyte Bearing Cretaceous Fault in the Saddlebag Lake Pendant, central Sierra Nevada. AGU Fall Meeting, CA Abstract T41B-2149.
Žák, J., Paterson, S.R., Memeti, V., 2007. Four magmatic fabrics in the Tuolumne batholith, central Sierra Nevada, California (USA): implications for interpreting fabric patterns in plutons and evolution of magma chambers in the upper crust. Geol. Soc. Am. Bull. 119 (½), 184–201. http://dx.doi.org/10.1130/B25773.